Sensitivity of Modeled Elastic Deformation in the Amundsen Sea Embayment

Jasmine S Hansen[1], William J Dukin[2], Michael J Willis[3], Terry J. Wilson[2], Michael G. Bevis[2], and Demián D Gómez[2]

[1]University of Colorado Boulder
[2]Ohio State University
[3]Virgina Tech

February 27, 2023

Abstract

This study investigates the effects of using high resolution surface load change grids when modeling elastic crusted deformation at ANET-POLENET Global Navigation Satellite System (GNSS) sites in the Amundsen Sea Embayment (ASE), Antarctica. We create sub-kilometer resolution surface change grids from 1143 digital elevation models (DEMs) derived from stereo optical imagery. We model elastic deformation at grid resolutions between 0.32 and 6 km. We find that grid resolutions of 6 km are appropriate to characterize elastic deformation at the ANET-POLENET sites within the ASE, as each GNSS site is more than 5 km from sites of major mass loss. Our experiments reveal that for localities where major mass change is occur within 5 km, such as at grounding zones and shear margins, the effects of surface load grid resolution within elastic models may be large and finer scale resolutions (less than 0.32 km) should be used.

Sensitivity of Modeled Elastic Deformation in the Amundsen Sea Embayment

J. S. Hansen[1,2], W. J. Durkin[3], M. J. Willis[1,2,4], T. J. Wilson[3], M. G. Bevis[3], D. D. Gómez[3]

[1]Department of Geological Sciences, University of Colorado Boulder [2]Cooperative Institute for Research in Environmental Sciences [3]School of Earth Sciences, The Ohio State University [4]Department of Geosciences, Virginia Tech

Corresponding author: Jasmine Hansen (jasmine.hansen@colorado.edu)

Key Points:

- High resolution grids of surface load change are not required to accurately model elastic deformation at GNSS sites in the ASE, Antarctica
- This is because each GNSS site is situated > 5 km away from large massd loss sites in the ASE including the Pine Island and Kohler Glaciers
- Previous estimates of GNSS residuals in the ASE are appropriate to calibrate GIA models and remove solid Earth effects from gravimetric data

Abstract

This study investigates the effects of using high resolution surface load change grids when modeling elastic crustal deformation at ANET-POLENET Global Navigation Satellite System (GNSS) sites in the Amundsen Sea Embayment (ASE), Antarctica. We create sub-kilometer resolution surface change grids from 1143 digital elevation models (DEMs) derived from stereo optical imagery. We model elastic deformation at grid resolutions between 0.32 and 6 km. We find that grid resolutions of 6 km are appropriate to characterize elastic deformation at the ANET-POLENET sites within the ASE, as each GNSS site is situated more than 5 km from major mass loss. Our experiments reveal that for localities where major mass change is occurring within 5 km, such as at grounding zones and shear margins, the effects of surface load grid resolution within elastic models may be large and finer scale resolutions (less than 0.32 km) should be used.

Plain Language Summary

Continuously operating GNSS sites within the Amundsen Sea Embayment record the response of the Earth's crust and mantle to the transfer of ice from the West Antarctic Ice Sheet into the ocean. To understand how this motion may impact future ice sheet retreat patterns it is necessary to separate the elastic deformation of the crust from viscoelastic motion occurring within the Earth's mantle. This is commonly achieved by the use of elastic models that model the response of the Earth to surface mass change grids. In this study we assess how varying the spatial resolution of these grids impacts elastic model results using custom built sub-kilometer resolution grids derived from DEMs. We find that that the GNSS sites within our study region are too far away from large ice changes to require a local, high-resolution loading grid. However, localities elsewhere that are within 5 km of large mass changes, such as those occurring at grounding zones and glacier margins, may be at risk of high levels of uncertainty in modeled elastic estimates. These findings are important to ensure that glacial isostatic adjustment (GIA) models are appropriately calibrated and gravimetric measurements of ice sheet mass loss are robust.

1 Introduction

The glaciers within the Amundsen Sea Embayment (ASE) region provide 92% of the mass lost from the West Antarctic Ice Sheet (WAIS), which has lost mass at a rate of over 125 Gt/yr between 2002 and 2019 (Rignot et al., 2019; Velicogna et al., 2020). The dominant source of loss originates from the widespread thinning of the Pine Island, Thwaites, Smith, Pope, Kohler and Haynes glaciers (Figure 1), that combined hold approximately 125 cm of Sea Level Equivalent (Bamber et al., 2019; Bamber & Dawson, 2020; Rignot et al., 2019; Milillo et al., 2022). The WAIS has long been identified as particularly vulnerable to accelerated mass loss (Hughes, 1981) in part due to the presence of a retrograde bed-slope beneath the ice sheet that may drive future catastrophic acceleration in grounding line retreat (Schoof, 2007; Weertman, 1974). Recent investigations have suggested that rapid solid Earth uplift, occurring in response to the extensive regional ice mass loss, may have the potential to contribute to stabilization of the WAIS resulting from a solid-Earth ice sheet feedback mechanism (Barletta et al., 2018; Gomez et al., 2015). This rapid uplift is driven by a combination of elastic flexure of the crust, and rapid deformation of a low viscosity upper mantle that responds on decadal timescales (Barletta et al., 2018; Coulon et al., 2021).

Although viscoelastic deformation is thought to be the major driver of motion within the ASE region, elastic deformation can represent over 20 % of the uplift signal in the ASE region (Barletta et al., 2018). Therefore, any inaccuracies introduced when modeling and estimating elastic deformation will result in non-negligible effects on glacial isostatic adjustment (GIA) model solutions and mantle viscosity estimates for the ASE region (Barletta et al. 2018). Recent studies conducted in the ASE have shown that the representation of surface mass change patterns within solid Earth models can introduce previously unmodeled variations in elastic and viscoelastic estimates (Larour et al., 2019; Kjeldsen et al., 2020; Wan et al., 2022). Larour et al. (2019) find that these variations can compound over time, resulting in a large spread of output scenarios predicting future sea level change. The topic of surface load representation within

elastic models and their potential affects on ANET-POLENET sites is also raised by Bamber and Dawson (2020).

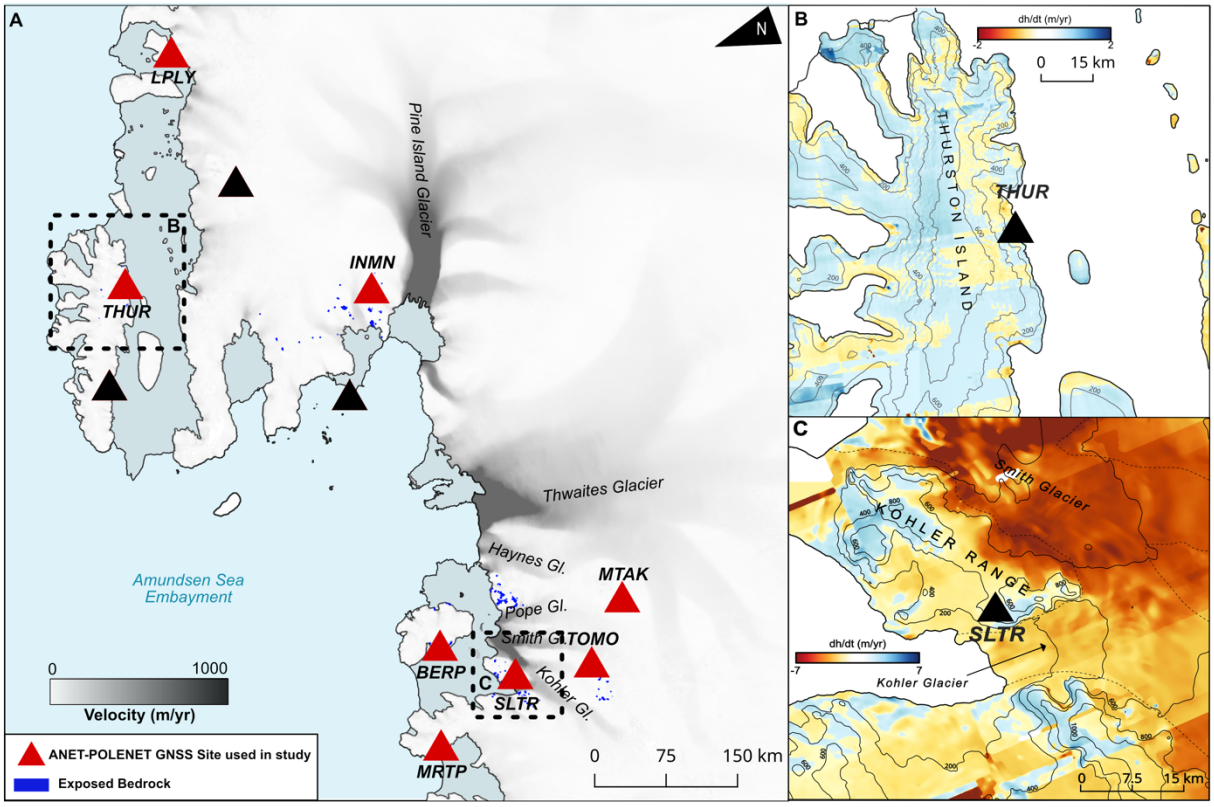

Figure 1. (a) ANET-POLENET GNSS sites indicated with red triangles are used in this study. Black triangles indicate sites excluded from this study due to a lack of available surface change data. High velocity regions (Mouginot et al. 2012; Rignot et al. 2011) are indicated in dark grey and blue outlines show the sparse availability of bedrock points in the ASE region. (b) Surface elevation changes derived from timeseries REMA data over Thurston Island showing low magnitude surface changes. (c) REMA derived dh/dt indicates differential surface lowering of the Smith and Kohler Glaciers, and surface height increases over the Kohler Mountain Range

In this study we investigate the effects of surface load change grid resolution when modeling elastic deformation in the ASE region. We use surface change grids, developed using digital elevation models (DEMs) derived from stereo optical satellite imagery (Howat et al., 2019), to assess how varying the grid resolution impacts output elastic deformation values. We calculate

deformation at four grid resolutions at eight bedrock mounted ANET-POLENET GNSS stations in the ASE region that are used as vital calibrations for Glacial Isostatic Adjustment (GIA) models (Barletta et al., 2018) (Figure 1). We also present the results of experiments to understand how grid resolution effects vary spatially and calculate viscoelastic motions for each GNSS site using updated velocity solutions.

Solid Earth deformation affects GIA models, which are, in turn used to correct gravimetric observations of ice mass change (Caron & Ivins, 2020). GIA models are calibrated with independent datasets, such as bedrock GNSS velocities to reduce uncertainties (Adhikari et al., 2021; Barletta et al., 2018; Martín-Español et al., 2016a, 2016b). The GNSS crustal deformation velocities must remove the elastic component to yield a viscoelastic residual signal that is representative of the viscoelastic, sub-crustal earth deformation (Barletta et al., 2018). Improving elastic model inputs will better constrain gravimetrically derived estimates of contemporary ice mass loss, such as those from the Gravity Recovery And Climate Experiment (GRACE) and GRACE Follow On (GRACE-FO) missions (Tapley et al., 2019; Velicogna et al., 2020). In Greenland, a reduction of the 3.4 ± 1.9 mm/yr offset between GIA model predictions and GNSS vertical motion values (Adhikari et al., 2021) increases GRACE mass loss estimates of the Greenland Ice Sheet by more than 10%.

2 Data and Methods

2.1 Surface Change Grids

We derived grids of surface elevation change at 30 m resolution using 1143 2 m posted DEM strips. DEM strips are publicly available as part of the Reference Elevation Model of Antarctica (REMA) and are produced from sub-meter resolution satellite imagery using the SETSM open-source package (Howat et al., 2019). Errors in the initial geolocation of the DEMs during their production can result in mismatches when comparing pixel locations to geolocated coordinates (Dai & Howat, 2017; Howat et al., 2019). To reduce biases it is necessary to coregister each DEM strip to a reference point cloud, a process which has been shown to improve geolocation (Noh & Howat, 2015). We create a custom reference point cloud to coregister our DEM strips. In Antarctic

112 regions such as the ASE, a lack of exposed bedrock limits the quantity of static reference
113 points available to robustly coregister DEM strips (Shean et al., 2019). We therefore
114 produce a reference point cloud that consists of both static (such as bedrock) and near-
115 static points to increase available tie point locations, modifying a method employed by
116 Shean et al. (2019). To identify near-static points we use long term horizontal and vertical
117 velocity datasets from MEaSURes (Mouginot et al., 2012; Rignot et al., 2011) and
118 ICESat-2 respectively (Smith et al. 2020) that are hosted within Google Earth Engine.
119 For MEaSURes data we isolate points with rates of horizontal motion of < 10 m/yr. For
120 ICESat2 we use a threshold of < 0.5 m/yr. The horizontal and vertical velocity masks are
121 intersected and combined with a mask of bedrock (static) locations. The resulting mask is
122 applied to REMA tiles (REFs) to produce a reference elevation point cloud. For more
123 detail and uncertainties please see Supporting Information.

124 DEM strips were coregistered to the reference point cloud using the iterative closest point
125 algorithm within the NASA Ames Stereo Pipeline and DEMCOREG packages (Shean et
126 al., 2016). The open source Cryosphere and Remote Sensing Toolkit (CARST) (Zheng et
127 al., 2018) was then used to assess coregistration uncertainties. We obtained the difference
128 in elevation between each DEM strip and the reference point cloud and calculated the
129 standard deviation after iteratively clipping outliers > 3 median absolute deviation away
130 from the mean (Zheng et al., 2018). We then discarded DEM strips with an uncertainty of
131 > 4 m and mean point cloud offset of > 2m, yielding a total of 1143 useable DEMs. DEM
132 strips span the period between January 2011 - October 2019. We removed pixel regions
133 with an absolute elevation difference > 60 m from the reference cloud to eliminate values
134 associated with cloud cover (Shean et al., 2019). Finally, DEMs were clipped to the
135 coastline to isolate grounded ice using the coastline dataset from Gerrish et al. (2021) and
136 bilinearly interpolated to a common 30 m grid.

137 Average Eulerian surface elevation changes (dh/dt) (Figure 1) were calculated using the
138 CARST package, whereby a weighted linear regression was applied to a time-ordered
139 DEM stack on a pixel by pixel basis (Zheng et al., 2018). This regression was only
140 calculated if there are a minimum of 3 DEM values at a particular pixel location. Dh/dt
141 grids were then median filtered to remove spurious values and clipped to a 60 km radius

surrounding each GNSS site, to ensure that we are capturing any elastic signal with a spatial wavelength appropriate for the regional crustal thickness estimate (Barletta et al., 2018; Heeszel et al., 2016). Dh/dt uncertainty grids are provided in the Supporting Information.

2.2 Creating Grids for Elastic Modeling

Loading grids for elastic modeling were produced using the H3 hexagonal hierarchical geospatial indexing system - a discrete global grid system consisting of a multi-precision hexagonal tiling that provides large computational efficiencies (Uber Technologies Inc., 2023). We used the H3 system to arrange loading cells with rhombohedral packing, reducing gaps between adjacent cells when compared to simple cubic packing (Durkin et al., 2019). We nested each of our high resolution grids within the 10 km regional dh/dt solution of Schröder et al. (2019) to ensure that we included regional mass changes occurring over the same temporal scales.

Mass redistribution in the ASE can be attributed to two processes – changes in surface mass balance (SMB) and dynamic thinning (Shepherd et al., 2019). Generally dynamic thinning involves the redistribution of ice that has a greater density than the material transported via SMB processes (Schröder et al., 2019). When generating estimates of mass change, these variations in density must be accounted for. We converted dh/dt grids to mass change grids by multiplying each grid cell by a defined density value, identified by application of a velocity threshold of 55 m/yr (Schröder et al., 2019) extracted from a long term ice surface velocity dataset (Mouginot et al., 2012; Rignot et al., 2011). Locations with velocities above this threshold were assigned a density of ice (917 kg/m^3) and locations with slower velocities were assigned the lower density of 550 kg/m^3 (McMillan et al., 2014; Riva et al., 2009; Schröder et al., 2019). We did not use surface change models such as the IMAU Firn Densification Model (Ligtenberg et al., 2011) or Community Firn Model (Stevens et al., 2020) to convert to mass since their coarse resolution results in the removal of short spatial wavelength surface change patterns. We calculate two additional density scenarios (provided in the Supporting Information) where all elevation changes are attributed to either ice or snow. We observe consistent

171 resolution dependent effects across every scenario and therefore focus on presenting our
172 velocity threshold solution for the remainder of the manuscript.
173
174 2.3 Elastic Modeling
175
176 Elastic parameter profiles were compiled using solid Earth models specific to Antarctica.
177 For the mantle we used the ANT-20 tomographic model (Lloyd et al., 2020) to extract Vs
178 (s wave velocity) and Vp (p wave velocity) and estimated mantle density from Pappa et
179 al. (2019). For regions in the mantle that are deeper than regions represented in the Lloyd
180 et al. (2020) and Pappa et al. (2019) models we used values from the Preliminary
181 Reference Earth Model (PREM) (Dziewonski & Anderson, 1981). Vs for the crustal
182 layers was extracted from the surface wave model of Zhou et al. (2022). Crustal Vp and
183 density were then estimated from the crustal Vs using the empirical relations of Brocher
184 (2005). These datasets were sampled onto a common grid using the H3 grid system at the
185 R3 resolution which is approximately equal to 1 degree (Brodsky, 2018). Load Love
186 number solutions to the equations of motion were calculated using the open source giapy
187 package (Kachuck, 2017) from the core-mantle boundary to the Earth surface (Durkin et
188 al., 2019). We used a harmonic order of 250,000, appropriate for modeling elastic
189 deformation with cell radii down to 160 m, to prevent truncation errors in the Green's
190 Functions (Bevis et al., 2016). Using higher harmonic orders did not result in significant
191 variations in our modeling estimates and decreases computational efficiency (see
192 Supporting Information). We repeated this procedure for 1000 randomly selected elastic
193 parameter profiles. Green's function computations and convolution of cell loads in the
194 space-domain were performed using the Regional ElAstic Rebound Calculator (REAR)
195 (Melini et al., 2018) and load Love numbers computed from the giapy algorithm
196 (Kachuck, 2017; Melini et al., 2018). From our 1000 runs we calculated the average and
197 standard deviation of the output elastic deformation rates to account for uncertainties
198 resulting from the use of a 1D earth model (Adhikari et al., 2021; Durkin et al., 2019).
199 We repeated this modeling procedure, resampling the high resolution surface change
200 solution at four different grid resolutions (6 km, 2.27 km, 0.86 km, and 0.32 km) whereby

distances correspond to the length (or diameter) of a square cell with the same area as the corresponding hexagon size (Brodsky, 2018).

2.5 Location Sensitivity Experiments

We test for the importance of the distance between surface load change and location of measurement within an elastic model by generating elastic deformation profiles at our four differing grid resolutions. Previous studies have shown that the greater the distance between the two the lower the recorded deformation (Wahr et al., 2013). However, how the magnitude and pattern of this decay varies with grid resolutions below 1 km remained unclear. We conduct these experiments by calculating vertical modeled elastic uplift at a fixed origin point as a surface loading disc is moved increasing distances away. As the cell is moved outwards from the origin by 1/3 of its radius, deformation at the origin is recorded until the cell is 10 degrees away from the origin location, producing a deformation profile. We repeat this experiment using cell diameters of 6, 2.27, 0.86 and 0.32 km (equal to those used when calculating elastic deformation at our GNSS sites). To ensure we are isolating the effects of grid resolution, the mass of the cell used remains constant for each resolution experiment.

2.6 GNSS Solutions

ANET-POLENET data was processed within a global network composed of ~2500 stations (using data spanning 1993 – 2022) using a parallelized Python wrapper for GAMIT/GLOBK v10.71 (Gómez et al., 2023). Atmospheric delays are estimated using the Vienna Mapping Functions (Boehm et al., 2006), and the effect of ocean tides accounted for by use of the FES2014b model (Lyard et al., 2021). An automated procedure was used to fit trajectory models to the displacement timeseries of each GNSS station (Bevis & Brown, 2014; Bevis et al., 2019). Seasonal displacement cycles are modeled using a 4-term Fourier series and the approach of Bevis et al. (2019) utilized to model deformation transients. Reference frame realization and trajectory modeling is implemented simultaneously to ensure internal geometrical consistency (Bevis & Brown,

2014). Many stations located along the Amundsen Sea coast have timeseries that contain artifacts related to antenna and radome icing. We mitigate these large and highly systematic errors by conducting a customized analysis, remodeling the timeseries and fine-tuning the trajectory models (Table S2). For more detailed information regarding GNSS processing please see Supporting Information.

3 Results

3.1 Elastic Deformation

We focus on the vertical component of elastic deformation, which is used as the primary calibration metric for GIA models and shows the greatest variation in magnitude when varying grid resolution. Horizontal components are provided in the Supporting Information. Modeled vertical elastic deformation rates at each GNSS site are provided for the four surface load grid resolution solutions (Table 1). We observe sub-millimeter variations in elastic response when using input surface load grids with between 0.32 and 6 km resolution (Figure 2). At four GNSS sites - TOMO, BERP, SLTR, and INMN - the spread in vertical elastic motion is statistically insignificant as the variation falls within the error bounds of our elastic solutions (Figure 2). Of the four remaining sites the location with the greatest spread is Martin Peninsula (MRTP), where the solution varies by 0.41 ± 0.36 mm/yr. Our average elastic solutions (RAv_e) for each site fall within 2

mm/yr of previously published solutions for GNSS sites in the region (Table 1) (Barletta et al. 2018; Caron et al. 2018).

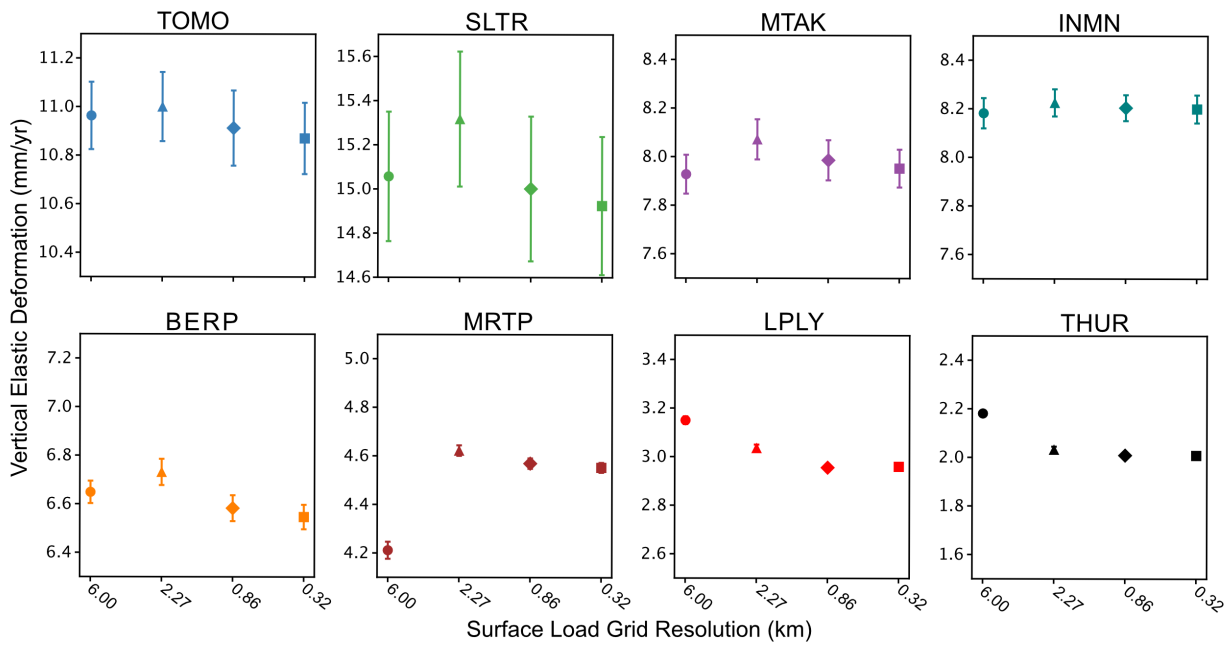

Figure 2. Vertical elastic deformation modeled at each GNSS site for each surface load grid resolution used within our elastic model. Uncertainty bounds are calculated from the standard deviation of the 1000 elastic model runs to account for the uncertainties associated with the use of a 1D earth profile.

Table 1. Vertical elastic deformation estimates and uncertainties for each grid resolution R6 (6 km), R7 (2.27 km), R8 (0.86 km), R9 (0.32 km), and elastic estimates from Barletta et al. (2018) (B_e) and Caron et al. (2018) (C_e). Updated GNSS vertical velocity solutions are provided and residual vertical velocities calculated by removing the average elastic uplift value (R_{Ave}).

	TOMO	BERP	SLTR	MTAK	MRTP	INMN	THUR	LPLY
$R6_e$ [mm/yr]	10.96 ± 0.14	6.65 ± 0.05	15.06 ± 0.29	7.93 ± 0.08	4.21 ± 0.04	8.18 ± 0.06	2.18 ± 0.01	3.15 ± 0.02
$R7_e$ [mm/yr]	11.00 ± 0.14	6.73 ± 0.05	15.32 ± 0.31	8.07 ± 0.08	4.62 ± 0.02	8.22 ± 0.06	2.03 ± 0.01	3.04 ± 0.01
$R8_e$ [mm/yr]	10.91 ± 0.15	6.58 ± 0.05	15.00 ± 0.33	7.99 ± 0.08	4.57 ± 0.02	8.20 ± 0.05	2.01 ± 0.01	2.96 ± 0.01
$R9_e$ [mm/yr]	10.87 ± 0.15	6.55 ± 0.05	14.92 ± 0.31	7.95 ± 0.08	4.55 ± 0.02	8.20 ± 0.06	2.01 ± 0.01	2.96 ± 0.01
RAv_e [mm/yr]	10.94 ± 0.15	6.63 ± 0.05	15.08 ± 0.31	7.98 ± 0.08	4.49 ± 0.02	8.20 ± 0.06	2.06 ± 0.01	3.03 ± 0.01
B_e [mm/yr]	10.7 ± 3.00	6.48 ± 0.7				9.15 ± 2.4	1.79 + 0.8	0.26 ± 0.5
C_e [mm/yr]	12.03	6.46					2.65	4.11
GNSS Uplift Rate [mm/yr]	59.49 ± 0.46	26.67 ± 0.12	49.65 ± 1.00	43.94 ± 0.89	14.12 ± 0.57	31.81 ± 0.38	-2.86 ± 0.11	5.24 ± 0.30
GNSS Residual [mm/yr]	48.55 ± 0.61	20.04 ± 0.17	34.57 ± 1.31	35.96 ± 0.97	9.63 ± 0.59	23.61 ± 0.44	-4.92 ± 0.12	2.21 ± 0.31

265

266 ### 3.2 GNSS Viscoelastic Residuals

267 We use our modeled average vertical elastic deformation rates (RAv_e) with our updated
268 GNSS solutions to calculate new GNSS residual estimates representing mantle-driven
269 viscoelastic GIA velocities. Vertical GNSS residuals are in excess of 20 mm/yr at five
270 GNSS stations, with the greatest rates located at the TOMO and MTAK (48.55 ± 0.61
271 mm/yr and 35.96 ± 0.97 mm/yr respectively. We derive the first residual vertical motion
272 values for 3 sites, of 34.57 ± 1.31 mm/yr (SLTR), 9.63 ± 0.59 mm/yr (MRTP) and 35.96
273 ± 0.97 mm/yr (MTAK). These high values are consistent with the model inference of
274 low viscosity mantle in the ASE region (Barletta et al., 2018).

275 ### 3.3 Location Sensitivity Experiments

276 Our location sensitivity experiments (detailed in section 2.5) show that there is a large
277 spread in modeled vertical elastic motion when loading discs of varying diameters are
278 close to the origin point (Figure 3). When the centroid of a 6 km diameter load cell is
279 placed at the origin, the modeled response at the origin is - 0.4 mm. We observe elastic
280 displacement over 30 times greater when repeating this experiment using a loading disc
281 of the same volume but with a cell diameter of 0.86 km (-16.33 mm). When the location
282 of the loading cell is moved away from the origin point the effects of disc diameter

283 decrease, before disappearing completely by ~ 5 km (Figure 3). We refer to this
284 approximate 5 km radius around the origin as the 'Zone of Sensitivity'.

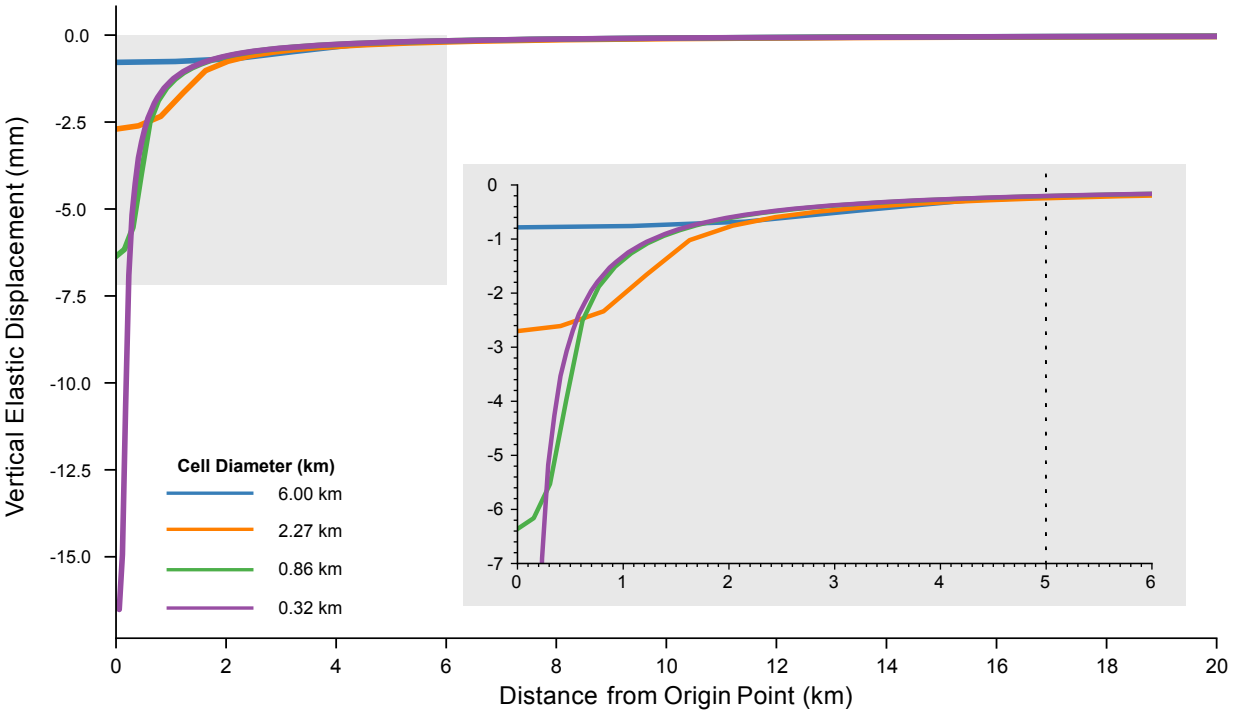

285

286

287 **Figure 3.** Profiles of vertical elastic deformation produced at each of the four surface load grid
288 resolutions generated by placing a load cell of fixed mass at increasing distance away from an
289 origin point. Inset graph provides an enlargement to better visualize variation in elastic
290 deformation occurring close to the origin point. The black dashed line shows the 5 km 'Zone of
291 Sensitivity' boundary.

292

293 **4 Discussion**

294 Sub-millimeter variations in modeled vertical elastic motion are observed when varying surface
295 grid resolutions between 0.32 and 6 km at GNSS sites within our study. At many sites these
296 variations fall within the error bounds of the elastic solutions, suggesting surface load grid
297 resolution is not strongly impacting modeled elastic estimates (Table 1). As a result of these
298 findings we suggest that ice dh/dt grid resolutions in excess of 6 km are presently sufficient for
299 modeling elastic deformation at GNSS sites in the ASE. Therefore, previously estimated ANET-

POLENT GNSS viscoelastic residuals, such as those of Barletta et al. (2018), are suitable to calibrate GIA model solutions and account for solid Earth motion in GRACE and GRACE-FO estimates of ice mass loss (Tapley et al., 2019; Velicogna et al., 2020).

This lack of variation when changing surface load grid resolution can be explained by the results of our location sensitivity experiments that show the decreasing influence of surface load grid resolution beyond 5 km from an origin point, or observation location. Isolating surface height changes (dh/dt) within this 'Zone of Sensitivity' at each GNSS site reveals that change rates are on average less than 1 m/yr. Intersecting this radius with our velocity threshold mask (Section x.x) shows that these changes are predominantly driven by SMB variations as opposed to dynamic thinning. Two GNSS sites within our study (INMN and SLTR) are situated near the grounding zone of major outlet glaciers where the greatest rates of grounded ice mass loss are observed (Bamber & Dawson, 2020; Milillo et al., 2022). INMN, near Pine Island Glacier, has been previously identified as being at risk for surface load grid resolution effects (Bamber & Dawson, 2020). We suggest that INMN is not presently at risk because the margin of Pine Island Glacier is located far outside of the sites 'Zone of Sensitivity'. This is also the case for SLTR that, although adjacent to the Kohler Glacier, is still situated farther than 5 km away from the glacier margin (Figure 1). Ice mass loss patterns within the ASE are evolving rapidly (Bamber & Dawson, 2020; Milillo et al., 2022), a trend that is predicted to continue. We therefore suggest it will be necessary to regularly re-evaluate the magnitude of mass changes within the 'Zone of Sensitivity' of INMN and SLTR, as well as those situated in the upper portion of glacier catchments such as TOMO and MRTP. This re-evaluation will be particularly important when modeling over extended temporal scales where ice mass loss patterns can evolve extensively through the modeling period (Larour et al., 2019)

Although our study is primarily focused on assessing uncertainties at ANET-POLENET ASE GNSS sites we suggest that the 'Zone of Sensitivity' concept may be a valuable tool when assessing the accuracy of gridded vertical elastic motion estimates, such as those used to correct dh/dt estimates (Smith et al., 2020). In these grids elastic deformation is calculated at many locations that would be affected by surface load change grid resolution, such as glacier margins and grounding zones where large surface changes fall within 5 km introducing unknown levels

of uncertainty. Furthermore, due to strong spatial control of surface load change grid resolution it may be possible to appropriately model gridded elastic deformation using a mixed resolution grid significantly improving computational speeds of large modeling frameworks

5 Conclusions

In this study we show that high resolution surface load change grids are not required to appropriately model vertical elastic deformation at current ANET-POLENET GNSS sites in the Amundsen Sea Embayment. Varying surface mass change grid resolutions down to 0.32 km resulted in vertical deformation variations of less than 0.5 mm/yr, with the values even smaller in the horizontal component. This small variation is explained by the relatively large spatial distances between the GNSS sites and the locations of major surface load changes, as demonstrated here by elastic deformation profiles that define a 'Zone of Sensitivity' of approximately 5 km surrounding a fixed location. Within this zone it is necessary to model the elastic response using high resolution surface mass load change grids. All current ANET-POLENT GNSS sites in the ASE region are located more than 5 km away from presently dominant changes in mass, and therefore are not sensitive to surface load change grid resolution solutions below 6 km in resolution. In contrast, the effects of surface load grid resolution are shown to be important at localities with high magnitude surface gradient changes occurring within 5 km. The results of this study and the identification of the 5 km 'Zone of Sensitivity' provide a potential framework to assess the uncertainty introduced by surface load grid resolution within elastic models and guide the creation of mixed resolution surface load change grids.

Acknowledgments

The authors declare that there are no conflicts of interest. This work was supported by NSF award numbers 0632322, 1249631, and 1745074 to the Ohio State University. Jasmine S. Hansen was supported by NASA Future Investigators in Earth Science grant 80NSSC20K1637. William J. Durkin was supported by the Byrd Postdoctoral Fellowship and NSF award 1745074. Geodetic data processing and trajectory analysis was completed at the Ohio State University by Michael Bevis, Demián Gómez, Eric Kendrick and David Saddler. We would also like to thank Stephanie Konfal and Whyjay Zheng for their assistance with this project.

Open Research

REMA data was provided by the Byrd Polar and Climate Research Center and the Polar Geospatial Center under NSF-OPP awards 1543501, 1810976, 1542736, 1559691, 1043681, 1541332, 0753663, 1548562, 1238993 and NASA award NNX10AN61G. Computer time provided through a Blue Waters Innovation Initiative. DEMs produced using data from Maxar DigitalGlobe, Inc. Altimtery data from Schröder et al. (2019) is available on PANGAEA (https://doi.org/10.1594/PANGAEA.897390). Ice velocity data is available at the National Snow and Ice Data Center (NSIDC) (https://nsidc.org/data/NSIDC-0484/versions/2) and surface elevation change from Smith et al. (2020). To process our DEM timeseries we used DEMCOREG (https://github.com/dshean/demcoreg), NASA Ames Stereo Pipeline (https://ti.arc.nasa.gov/tech/asr/groups/intelligent-robotics/ngt/stereo/), CARST (http://doi.org/10.5281/zenodo.3475693), and H3 (https://github.com/uber/h3). To calculate elastic deformation we use the packages giapy (Kachuck, 2017) and REAR (Melini et al., 2014) which are available at http://hpc.rm.ingv.it/rear/ and https://github.com/skachuck/giapy. Elastic deformation data from Caron et al. (2018) was provided upon request by L. Caron & S. Adhikari. GNSS solutions were processed by The Ohio State University from RINEX data available from UNAVCO (https://data.unavco.org/archive/gnss/rinex/obs.) and using Parallel.GAMIT (https://github.com/demiangomez/Parallel.GAMIT). Code to build surface change grids and output elastic deformation results can be found at https://github.com/jaha2600/ase_elastic_grl_2023/. Surface change grids and elastic model results are available at https://doi.org/10.5281/zenodo.7658864

References

Adhikari, S., Milne, G. A., Caron, L., Khan, S. A., Kjeldsen, K. K., Nilsson, J., et al. (2021). Decadal to Centennial Timescale Mantle Viscosity Inferred from Modern Crustal Uplift Rates in Greenland. *Geophysical Research Letters*, *48*(19), https://doi.org/10.1029/2021gl094040

Bamber, J. L., Oppenheimer, M., Kopp, R. E., Aspinall, W. P., & Cooke, R. M. (2019). Ice sheet contributions to future sea-level rise from structured expert judgment. *Proceedings of the National Academy of Sciences*, *116*(23), 11195-11200. https://doi.org/10.1073/pnas.1817205116

Bamber, J. L., & Dawson, G. J. (2020). Complex evolving patterns of mass loss from Antarctica's largest glacier. *Nature Geoscience*, *13*(2), 127–131. https://doi.org/10.1038/s*41*561-019-0527-z

Barletta, V. R., Bevis, M., Smith, B. E., Wilson, T., Brown, A., Bordoni, A., et al. (2018). Observed rapid bedrock uplift in Amundsen Sea Embayment promotes ice-sheet stability. *Science*, *360*(6395), 1335–1339. https://doi.org/10.1126/science.aao1*447*

Bevis M., Brown, A., & Kendrick, E. (2013). Devising stable geometrical reference frames for use in geodetic studies of vertical crustal motion, *Journal of Geodesy,* 87, 311-321, https://doi.org/10.1007/s00190-012-0600-5.

Bevis, M., & Brown, A. (2014). Trajectory models and reference frames for crustal motion geodesy, *Journal of Geodesy*, 88, 283-311. https://doi.org/10.1007/s00190-013-0685-5

Bevis, M., Melini, D., & Spada, G. (2016). On computing the geoelastic response to a disk load. *Geophysical Journal International*, *205*(3), 1804–1812. https://doi.org/10.1093/gji/ggw115

Bevis, M., Bedford, J., & Caccamise II, D. (2019). The art and science of trajectory modeling. In J-P. Montillet, M. Bos (Eds.), *Geodetic Time Series Analysis in Earth Sciences* (pp. 1-28) https://doi.org/10.1007/978-3-030-21718-1_1.

Boehm, J., Niell, A., Tregoning, P., & Schuh, H. (2006). Global Mapping Function (GMF): A new empirical mapping function based on numerical weather model data. *Geophysical Research Letters, 33*(7), https://doi.org/10.1029/2005GL025546

Brocher, T. M. (2005). Empirical Relations between Elastic Wavespeeds and Density in the Earth's Crust. *Bulletin of the Seismological Society of America*, *95*(6), 2081–2092. https://doi.org/10.1785/0120050077

Caron, L., Ivins, E. R., Larour, E., Adhikari, S., Nilsson, J., & Blewitt, G. (2018). GIA Model Statistics for GRACE Hydrology, Cryosphere, and Ocean Science. *Geophysical Research Letters*. *45*(5), 2203–2212. https://doi.org/10.1002/2017gl076644

Caron, Lambert, & Ivins, E. R. (2020). A baseline Antarctic GIA correction for space gravimetry. *Earth and Planetary Science Letters*, *531*. https://doi.org/10.1016/j.epsl.2019.115957

Coulon, V., Bulthuis, K., Whitehouse, P. L., Sun, S., Haubner, K., Zipf, L., & Pattyn, F. (2021). Contrasting Response of West and East Antarctic Ice Sheets to Glacial Isostatic Adjustment. *Journal of Geophysical Research: Earth Surface*, *126*(7). https://doi.org/10.1029/2020jf006003

Dai, C., & Howat, I. M. (2017). Measuring Lava Flows With ArcticDEM: Application to the 2012–2013 Eruption of Tolbachik, Kamchatka. *Geophysical Research Letters, 44*(24), 133-140. https://doi.org/10.1002/2017gl075920

Durkin, W., Kachuck, S., & Pritchard, M. (2019). The Importance of the Inelastic and Elastic Structures of the Crust in Constraining Glacial Density, Mass Change, and Isostatic Adjustment From Geodetic Observations in Southeast Alaska. *Journal of Geophysical Research: Solid Earth*, *126*(1), 1106-1119. https://doi.org/10.1029/2018jb016399

Dziewonski, A. M., & Anderson, D. L. (1981). Preliminary reference Earth model. *Physics of the Earth and Planetary Interiors*, *25*(4), 297–356. https://doi.org/10.1016/0031-9201(81)90046-7

Gerrish, L., Fretwell, P., & Cooper, P. (2021). High resolution vector polylines of the Antarctic coastline (Version 7.4) [Dataset]. NERC EDS UK Polar Data Centre. https://doi.org/10.5285/e46be5bc-ef8e-4fd5-967b-92863fbe2835

Gómez, D. (2023). Parallel.GAMIT. [Software]. GitHub. https://github.com/demiangomez/Parallel.GAMIT

Gomez, N., Pollard, D., & Holland, D. (2015). Sea-level feedback lowers projections of future Antarctic Ice-Sheet mass loss. *Nature Communications*, 6. https://doi.org/*10*.1038/ncomms9798

Heeszel, D. S., Wiens, D. A., Anandakrishnan, S., Aster, R. C., Dalziel, I. W. D., Huerta, A. D., et al. (2016). Upper mantle structure of central and West Antarctica from array analysis of Rayleigh wave phase velocities. *Journal of Geophysical Research: Solid Earth*, *121*(3), 1758–1775. https://doi.org/10.1002/2015jb012616

Howat, I. M., Porter, C., Smith, B. E., Noh, M.-J., & Morin, P. (2019). The Reference Elevation Model of Antarctica. *The Cryosphere*, *13*(2), 665–674. https://doi.org/10.5194/tc-13-665-2019

Hughes, T. J. (1981). The weak underbelly of the West Antarctic ice sheet. *Journal of Glaciology*, *27*(97), 518–525. https://doi.org/10.3189/s002214300001159x

Kachuck, S. B. (2017). giapy: Glacial Isostatic Adjustment in Python (Version 1.0.0) [Software]. GitHub. https://github.com/skachuck/giapy

Kjeldsen, K. K., Khan, S. A., Colgan, W. T., MacGregor, J. A., & Fausto, R. S. (2020). Time-Varying Ice Sheet Mask: Implications on Ice-Sheet Mass Balance and Crustal Uplift. *Journal of Geophysical Research: Earth Surface*, *125*(12). https://doi.org/10.1029/2020jf005775

Larour, E., Seroussi, H., Adhikari, S., Ivins, E., Caron, L., Morlighem, M., & Schlegel, N. (2019). Slowdown in Antarctic mass loss from solid Earth and sea-level feedbacks. *Science, 364*(6444), eaav7908. https://doi.org/10.1126/science.aav7908

Ligtenberg, S. R. M., Helsen, M. M., & Broeke, M. R. van den. (2011). An improved semi-empirical model for the densification of Antarctic firn. *The Cryosphere, 5*(4), 809–819. https://doi.org/10.5194/tc-5-809-2011

Liu, L., Khan, S. A., Dam, T., Ma, J. H. Y., & Bevis, M. (2017). Annual variations in GPS-

483 measured vertical displacements near Upernavik Isstrøm (Greenland) and contributions from
484 surface mass loading. *Journal of Geophysical Research: Solid Earth, 122*(1), 677–691.
485 https://doi.org/10.1002/2016jb013494
486
487 Lloyd, A. J., Wiens, D. A., Zhu, H., Tromp, J., Nyblade, A. A., Aster, R. C., et al. (2020).
488 Seismic Structure of the Antarctic Upper Mantle Imaged with Adjoint Tomography. *Journal of*
489 *Geophysical Research: Solid Earth, 125*(3). https://doi.org/10.1029/2019jb017823
490
491 Lyard, F. H., Allain, D. J., Cancet, M., Carrère, L., & Picot, N. (2021). FES2014 global ocean
492 tides atlas: design and performances. *Ocean Science, 17*(3),1–40. https://doi.org/10.5194/os-17-
493 615-2021
494
495 Martín-Español, A., King, M. A., Zammit-Mangion, A., Andrews, S. B., Moore, P., & Bamber,
496 J. L. (2016a). An assessment of forward and inverse GIA solutions for Antarctica. *Journal of*
497 *Geophysical Research: Solid Earth, 121*(9), 6947–6965. https://doi.org/10.1002/2016jb013154
498
499 Martín-Español, A., Zammit-Mangion, A., Clarke, P. J., Flament, T., Helm, V., King, M. A., et
500 al. (2016b). Spatial and temporal Antarctic Ice Sheet mass trends, glacio-isostatic adjustment,
501 and surface processes from a joint inversion of satellite altimeter, gravity, and GPS data. *Journal*
502 *of Geophysical Research: Earth Surface, 121*(2), 182–200. https://doi.org/10.1002/2015jf003550
503
504 McMillan, M., Shepherd, A., Sundal, A., Briggs, K., Muir, A., Ridout, A., et al. (2014).
505 Increased ice losses from Antarctica detected by CryoSat-2. *Geophysical Research Letters,*
506 *41*(11), 3899–3905. https://doi.org/10.1002/2014gl060111
507
508 Melini, D., Spada, G., Gegout, P., King, M., & Consorzi, A. (2018). REAR - A Regional Elastic
509 Rebound Calculator. (Verson 1.0.1) [Software]. GitHub. http://github.com/danielemelini/rear
510
511 Melkonian, A.K. (2014). *Quantifying and Characterizing Mass Loss From Icefields Using*
512 *Remote Sensing* (Doctoral dissertation). Retrieved from Cornell eCommons.

(https://hdl.handle.net/1813/39298) Ithaca, NY: Cornell University.

Milillo, P., Rignot, E., Rizzoli, P., Scheuchl, B., Mouginot, J., Bueso-Bello, J. L., et al. (2022). Rapid glacier retreat rates observed in West Antarctica. *Nature Geoscience, 15*(1), 48–53. https://doi.org/10.1038/s41561-021-00877-z

Mouginot, J., Scheuchl, B., & Rignot, E. (2012). Mapping of Ice Motion in Antarctica Using Synthetic-Aperture Radar Data. *Remote Sensing*, *4*(9), 2753–2767. https://doi.org/10.3390/rs4092753

Nilsson, J., Gardner, A., Sørensen, L. S., & Forsberg, R. (2016). Improved retrieval of land ice topography from CryoSat-2 data and its impact for volume-change estimation of the Greenland Ice Sheet. *The Cryosphere, 10*(6), 2953–2969. https://doi.org/10.5194/tc-10-2953-2016

Noh, M.-J., & Howat, I. M. (2015). Automated stereo-photogrammetric DEM generation at high latitudes: Surface Extraction with TIN-based Search-space Minimization (SETSM) validation and demonstration over glaciated regions. *GIScience & Remote Sensing*, *52*(2), 198–217. https://doi.org/10.1080/15481603.2015.1008621

Pappa, F., Ebbing, J., Ferraccioli, F., & Wal, W. (2019). Modeling Satellite Gravity Gradient Data to Derive Density, Temperature, and Viscosity Structure of the Antarctic Lithosphere. *Journal of Geophysical Research: Solid Earth, 124*(11), 12053–12076. https://doi.org/10.1029/2019jb017997

Rignot, E., Mouginot, J., & Scheuchl, B. (2011). Ice Flow of the Antarctic Ice Sheet. *Science, 333*(6048), 1427–1430. https://doi.org/10.1126/science.1208336

Rignot, E., J. Mouginot, & Scheuchl, B. (2017). MEaSUREs InSAR-Based Antarctica Ice Velocity Map (Version 2). [Dataset] NASA National Snow and Ice Data Center Distributed Active Archive Center. https://doi.org/10.5067/D7GK8F5J8M8R.

Rignot, Eric, Mouginot, J., Scheuchl, B., Broeke, M. van den, Wessem, M. J. van, & Morlighem, M. (2019). Four decades of Antarctic Ice Sheet mass balance from 1979–2017. *Proceedings of the National Academy of Sciences, 116*(4), 201812883. https://doi.org/10.1073/pnas.1812883116

Riva, R. E. M., Gunter, B. C., Urban, T. J., Vermeersen, B. L. A., Lindenbergh, R. C., Helsen, M. M., et al. (2009). Glacial Isostatic Adjustment over Antarctica from combined ICESat and GRACE satellite data. *Earth and Planetary Science Letters, 288*(3–4), 516–523. https://doi.org/10.1016/j.epsl.2009.10.013

Schoof, C. (2007). Ice sheet grounding line dynamics: Steady states, stability, and hysteresis. *Journal of Geophysical Research: Earth Surface*, *112*(F3). https://doi.org/10.1029/2006jf000664

Schröder, L., Horwath, M., Dietrich, R., Helm, V., Broeke, M. R. van den, & Ligtenberg, S. R. M. (2019). Four decades of Antarctic surface elevation changes from multi-mission satellite altimetry. *The Cryosphere, 13*(2), 427–449. https://doi.org/10.5194/tc-13-427-2019

Schröder, L., Horwath, M., Dietrich, R., Helm, V., Broeke, M. R. van den, & Ligtenberg, S. R. M. (2019). Gridded surface elevation changes from multi-mission satellite altimetry 1978-2017 [Dataset]. PANGAEA. https://doi.org/10.1594/PANGAEA.897390

Shean, D. E., Alexandrov, O., Moratto, Z. M., Smith, B. E., Joughin, I. R., Porter, C., & Morin, P. (2016). An automated, open-source pipeline for mass production of digital elevation models (DEMs) from very-high-resolution commercial stereo satellite imagery. *ISPRS Journal of Photogrammetry and Remote Sensing*, 116, 101–117. https://doi.org/10.1016/j.isprsjprs.2016.03.012

Shean, D. E., Joughin, I. R., Dutrieux, P., Smith, B. E., & Berthier, E. (2019). Ice shelf basal melt rates from a high-resolution digital elevation model (DEM) record for Pine Island Glacier, Antarctica. *The Cryosphere, 13*(10), 2633–2656. https://doi.org/10.5194/tc-13-2633-2019

Shepherd, A., Gilbert, L., Muir, A. S., Konrad, H., McMillan, M., Slater, T., et al. (2019). Trends in Antarctic Ice Sheet Elevation and Mass. *Geophysical Research Letters, 46*(14), 8174–8183. https://doi.org/10.1029/2019gl082182

Smith, B., Fricker, H. A., Gardner, A. S., Medley, B., Nilsson, J., Paolo, F. S., et al. (2020). Pervasive ice sheet mass loss reflects competing ocean and atmosphere processes. *Science, 367*(6496), 1239-1242. https://doi.org/10.1126/science.aaz5845

Stevens, C. M., Verjans, V., Lundin, J. M. D., Kahle, E. C., Horlings, A. N., Horlings, B. I., & Waddington, E. D. (2020). The Community Firn Model (CFM) v1.0. *Geoscientific Model Development*, *13*(9), 4355–4377. https://doi.org/10.5194/gmd-13-4355-2020

Tapley, B. D., Watkins, M. M., Flechtner, F., Reigber, C., Bettadpur, S., Rodell, M., et al. (2019). Contributions of GRACE to understanding climate change. *Nature Climate Change*, *9*(5), 358–369. https://doi.org/10.1038/s41558-019-0456-2

Uber Technologies Inc. (2023). H3: Hexagonal hierarchical geospatial indexing system (Version 3.5.0). [Software]. GitHub. https://github.com/uber/h3

Velicogna, I., Mohajerani, Y., A, G., Landerer, F., Mouginot, J., Noel, B., et al. (2020). Continuity of Ice Sheet Mass Loss in Greenland and Antarctica From the GRACE and GRACE Follow-On Missions. *Geophysical Research Letters, 47*(8). https://doi.org/10.1029/2020gl087291

Wahr, J., Khan, S. A., Dam, T., Liu, L., Angelen, J. H., Broeke, M. R., & Meertens, C. M. (2013). The use of GPS horizontals for loading studies, with applications to northern California and southeast Greenland. *Journal of Geophysical Research: Solid Earth, 118*(4), 1795-1806. https://doi.org/10.1002/jgrb.50104

603 Wan, J. X. W., Gomez, N., Latychev, K., & Han, H. K. (2022). Resolving glacial isostatic
604 adjustment (GIA) in response to modern and future ice loss at marine grounding lines in West
605 Antarctica. *The Cryosphere*, *16*(6), 2203-2223. https://doi.org/10.5194/tc-16-2203-2022
606
607 Weertman, J. (1974). Stability of the Junction of an Ice Sheet and an Ice Shelf. *Journal of*
608 *Glaciology, 13*(67), 3–11. https://doi.org/10.3189/s0022143000023327
609
610 Zheng, W., Pritchard, M. E., Willis, M. J., Tepes, P., Gourmelen, N., Benham, T. J., &
611 Dowdeswell, J. A. (2018). Accelerating glacier mass loss on Franz Josef Land, Russian Arctic.
612 *Remote Sensing of Environment*, 211, 357–375. https://doi.org/10.1016/j.rse.2018.04.004
613
614 Zheng, W., Durkin, W. J., Melkonian, A. K., & Pritchard, M. E. (2019). Cryosphere And Remote
615 Sensing Toolkit (CARST) v1.0.1 (Version v1.0.1) [Software]. Zenodo.
616 https://doi.org/10.5281/zenodo.3475693
617
618 Zhou, Z., Wiens, D. A., Shen, W., Aster, R. C., Nyblade, A., & Wilson, T. J. (2022). Radial
619 Anisotropy and sediment thickness of West and Central Antarctica estimated from Rayleigh and
620 Love wave velocities. *Journal of Geophysical Research: Solid Earth*, *127*(3).
621 https://doi.org/10.1029/2021JB022857

Sensitivity of Modeled Elastic Deformation in the Amundsen Sea Embayment

J. S. Hansen[1,2], W. J. Durkin[3], M. J. Willis[1,2,4], T. J. Wilson[3], M. G. Bevis[3], D. D. Gómez[3]

[1]Department of Geological Sciences, University of Colorado Boulder [2]Cooperative Institute for Research in Environmental Sciences [3]School of Earth Sciences, The Ohio State University [4]Department of Geosciences, Virginia Tech

Corresponding author: Jasmine Hansen (jasmine.hansen@colorado.edu)

Key Points:

- High resolution grids of surface load change are not required to accurately model elastic deformation at GNSS sites in the ASE, Antarctica
- This is because each GNSS site is situated > 5 km away from large massd loss sites in the ASE including the Pine Island and Kohler Glaciers
- Previous estimates of GNSS residuals in the ASE are appropriate to calibrate GIA models and remove solid Earth effects from gravimetric data

Abstract

This study investigates the effects of using high resolution surface load change grids when modeling elastic crustal deformation at ANET-POLENET Global Navigation Satellite System (GNSS) sites in the Amundsen Sea Embayment (ASE), Antarctica. We create sub-kilometer resolution surface change grids from 1143 digital elevation models (DEMs) derived from stereo optical imagery. We model elastic deformation at grid resolutions between 0.32 and 6 km. We find that grid resolutions of 6 km are appropriate to characterize elastic deformation at the ANET-POLENET sites within the ASE, as each GNSS site is situated more than 5 km from major mass loss. Our experiments reveal that for localities where major mass change is occurring within 5 km, such as at grounding zones and shear margins, the effects of surface load grid resolution within elastic models may be large and finer scale resolutions (less than 0.32 km) should be used.

Plain Language Summary

Continuously operating GNSS sites within the Amundsen Sea Embayment record the response of the Earth's crust and mantle to the transfer of ice from the West Antarctic Ice Sheet into the ocean. To understand how this motion may impact future ice sheet retreat patterns it is necessary to separate the elastic deformation of the crust from viscoelastic motion occurring within the Earth's mantle. This is commonly achieved by the use of elastic models that model the response of the Earth to surface mass change grids. In this study we assess how varying the spatial resolution of these grids impacts elastic model results using custom built sub-kilometer resolution grids derived from DEMs. We find that that the GNSS sites within our study region are too far away from large ice changes to require a local, high-resolution loading grid. However, localities elsewhere that are within 5 km of large mass changes, such as those occurring at grounding zones and glacier margins, may be at risk of high levels of uncertainty in modeled elastic estimates. These findings are important to ensure that glacial isostatic adjustment (GIA) models are appropriately calibrated and gravimetric measurements of ice sheet mass loss are robust.

1 Introduction

The glaciers within the Amundsen Sea Embayment (ASE) region provide 92% of the mass lost from the West Antarctic Ice Sheet (WAIS), which has lost mass at a rate of over 125 Gt/yr between 2002 and 2019 (Rignot et al., 2019; Velicogna et al., 2020). The dominant source of loss originates from the widespread thinning of the Pine Island, Thwaites, Smith, Pope, Kohler and Haynes glaciers (Figure 1), that combined hold approximately 125 cm of Sea Level Equivalent (Bamber et al., 2019; Bamber & Dawson, 2020; Rignot et al., 2019; Milillo et al., 2022). The WAIS has long been identified as particularly vulnerable to accelerated mass loss (Hughes, 1981) in part due to the presence of a retrograde bed-slope beneath the ice sheet that may drive future catastrophic acceleration in grounding line retreat (Schoof, 2007; Weertman, 1974). Recent investigations have suggested that rapid solid Earth uplift, occurring in response to the extensive regional ice mass loss, may have the potential to contribute to stabilization of the WAIS resulting from a solid-Earth ice sheet feedback mechanism (Barletta et al., 2018; Gomez et al., 2015). This rapid uplift is driven by a combination of elastic flexure of the crust, and rapid deformation of a low viscosity upper mantle that responds on decadal timescales (Barletta et al., 2018; Coulon et al., 2021).

Although viscoelastic deformation is thought to be the major driver of motion within the ASE region, elastic deformation can represent over 20 % of the uplift signal in the ASE region (Barletta et al., 2018). Therefore, any inaccuracies introduced when modeling and estimating elastic deformation will result in non-negligible effects on glacial isostatic adjustment (GIA) model solutions and mantle viscosity estimates for the ASE region (Barletta et al. 2018). Recent studies conducted in the ASE have shown that the representation of surface mass change patterns within solid Earth models can introduce previously unmodeled variations in elastic and viscoelastic estimates (Larour et al., 2019; Kjeldsen et al., 2020; Wan et al., 2022). Larour et al. (2019) find that these variations can compound over time, resulting in a large spread of output scenarios predicting future sea level change. The topic of surface load representation within

elastic models and their potential affects on ANET-POLENET sites is also raised by Bamber and Dawson (2020).

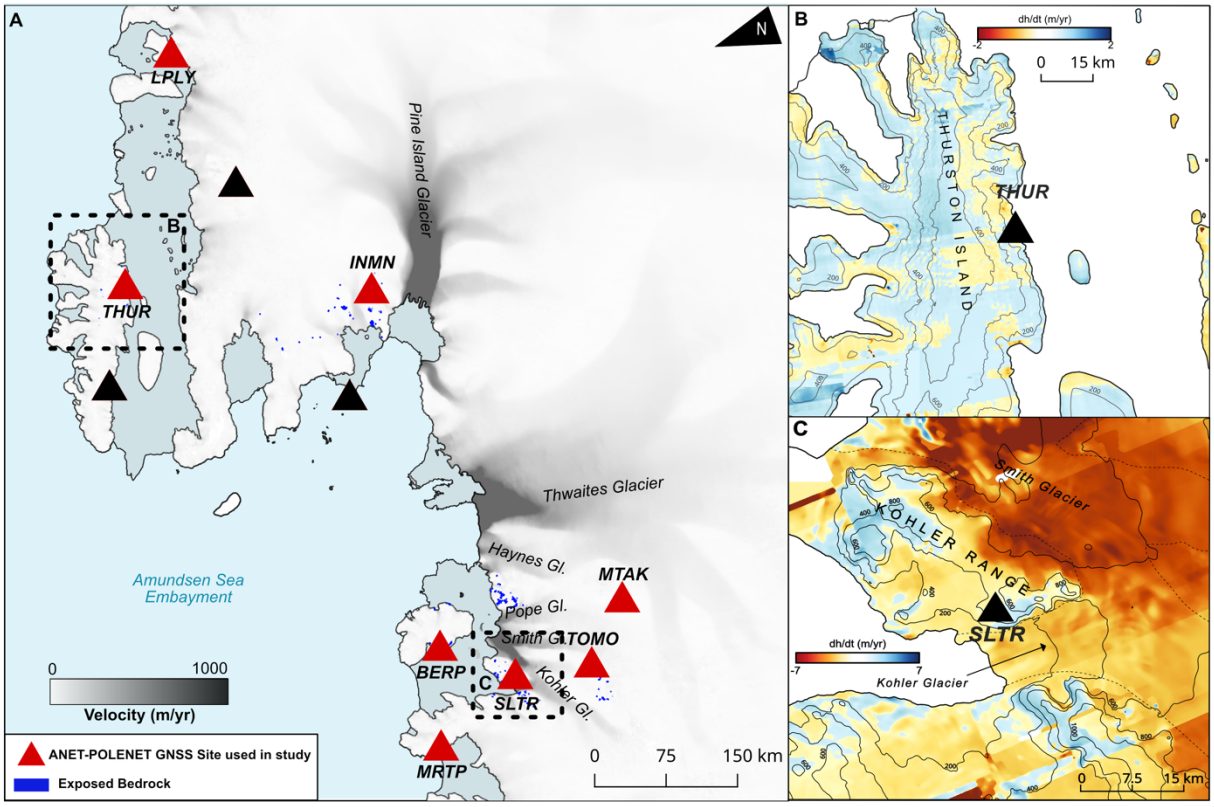

Figure 1. (a) ANET-POLENET GNSS sites indicated with red triangles are used in this study. Black triangles indicate sites excluded from this study due to a lack of available surface change data. High velocity regions (Mouginot et al. 2012; Rignot et al. 2011) are indicated in dark grey and blue outlines show the sparse availability of bedrock points in the ASE region. (b) Surface elevation changes derived from timeseries REMA data over Thurston Island showing low magnitude surface changes. (c) REMA derived dh/dt indicates differential surface lowering of the Smith and Kohler Glaciers, and surface height increases over the Kohler Mountain Range

In this study we investigate the effects of surface load change grid resolution when modeling elastic deformation in the ASE region. We use surface change grids, developed using digital elevation models (DEMs) derived from stereo optical satellite imagery (Howat et al., 2019), to assess how varying the grid resolution impacts output elastic deformation values. We calculate

deformation at four grid resolutions at eight bedrock mounted ANET-POLENET GNSS stations in the ASE region that are used as vital calibrations for Glacial Isostatic Adjustment (GIA) models (Barletta et al., 2018) (Figure 1). We also present the results of experiments to understand how grid resolution effects vary spatially and calculate viscoelastic motions for each GNSS site using updated velocity solutions.

Solid Earth deformation affects GIA models, which are, in turn used to correct gravimetric observations of ice mass change (Caron & Ivins, 2020). GIA models are calibrated with independent datasets, such as bedrock GNSS velocities to reduce uncertainties (Adhikari et al., 2021; Barletta et al., 2018; Martín-Español et al., 2016a, 2016b). The GNSS crustal deformation velocities must remove the elastic component to yield a viscoelastic residual signal that is representative of the viscoelastic, sub-crustal earth deformation (Barletta et al., 2018). Improving elastic model inputs will better constrain gravimetrically derived estimates of contemporary ice mass loss, such as those from the Gravity Recovery And Climate Experiment (GRACE) and GRACE Follow On (GRACE-FO) missions (Tapley et al., 2019; Velicogna et al., 2020). In Greenland, a reduction of the 3.4 ± 1.9 mm/yr offset between GIA model predictions and GNSS vertical motion values (Adhikari et al., 2021) increases GRACE mass loss estimates of the Greenland Ice Sheet by more than 10%.

2 Data and Methods

2.1 Surface Change Grids

We derived grids of surface elevation change at 30 m resolution using 1143 2 m posted DEM strips. DEM strips are publicly available as part of the Reference Elevation Model of Antarctica (REMA) and are produced from sub-meter resolution satellite imagery using the SETSM open-source package (Howat et al., 2019). Errors in the initial geolocation of the DEMs during their production can result in mismatches when comparing pixel locations to geolocated coordinates (Dai & Howat, 2017; Howat et al., 2019). To reduce biases it is necessary to coregister each DEM strip to a reference point cloud, a process which has been shown to improve geolocation (Noh & Howat, 2015). We create a custom reference point cloud to coregister our DEM strips. In Antarctic

112 regions such as the ASE, a lack of exposed bedrock limits the quantity of static reference
113 points available to robustly coregister DEM strips (Shean et al., 2019). We therefore
114 produce a reference point cloud that consists of both static (such as bedrock) and near-
115 static points to increase available tie point locations, modifying a method employed by
116 Shean et al. (2019). To identify near-static points we use long term horizontal and vertical
117 velocity datasets from MEaSURes (Mouginot et al., 2012; Rignot et al., 2011) and
118 ICESat-2 respectively (Smith et al. 2020) that are hosted within Google Earth Engine.
119 For MEaSURes data we isolate points with rates of horizontal motion of < 10 m/yr. For
120 ICESat2 we use a threshold of < 0.5 m/yr. The horizontal and vertical velocity masks are
121 intersected and combined with a mask of bedrock (static) locations. The resulting mask is
122 applied to REMA tiles (REFs) to produce a reference elevation point cloud. For more
123 detail and uncertainties please see Supporting Information.

124 DEM strips were coregistered to the reference point cloud using the iterative closest point
125 algorithm within the NASA Ames Stereo Pipeline and DEMCOREG packages (Shean et
126 al., 2016). The open source Cryosphere and Remote Sensing Toolkit (CARST) (Zheng et
127 al., 2018) was then used to assess coregistration uncertainties. We obtained the difference
128 in elevation between each DEM strip and the reference point cloud and calculated the
129 standard deviation after iteratively clipping outliers > 3 median absolute deviation away
130 from the mean (Zheng et al., 2018). We then discarded DEM strips with an uncertainty of
131 > 4 m and mean point cloud offset of > 2m, yielding a total of 1143 useable DEMs. DEM
132 strips span the period between January 2011 - October 2019. We removed pixel regions
133 with an absolute elevation difference > 60 m from the reference cloud to eliminate values
134 associated with cloud cover (Shean et al., 2019). Finally, DEMs were clipped to the
135 coastline to isolate grounded ice using the coastline dataset from Gerrish et al. (2021) and
136 bilinearly interpolated to a common 30 m grid.

137 Average Eulerian surface elevation changes (dh/dt) (Figure 1) were calculated using the
138 CARST package, whereby a weighted linear regression was applied to a time-ordered
139 DEM stack on a pixel by pixel basis (Zheng et al., 2018). This regression was only
140 calculated if there are a minimum of 3 DEM values at a particular pixel location. Dh/dt
141 grids were then median filtered to remove spurious values and clipped to a 60 km radius

surrounding each GNSS site, to ensure that we are capturing any elastic signal with a spatial wavelength appropriate for the regional crustal thickness estimate (Barletta et al., 2018; Heeszel et al., 2016). Dh/dt uncertainty grids are provided in the Supporting Information.

2.2 Creating Grids for Elastic Modeling

Loading grids for elastic modeling were produced using the H3 hexagonal hierarchical geospatial indexing system - a discrete global grid system consisting of a multi-precision hexagonal tiling that provides large computational efficiencies (Uber Technologies Inc., 2023). We used the H3 system to arrange loading cells with rhombohedral packing, reducing gaps between adjacent cells when compared to simple cubic packing (Durkin et al., 2019). We nested each of our high resolution grids within the 10 km regional dh/dt solution of Schröder et al. (2019) to ensure that we included regional mass changes occurring over the same temporal scales.

Mass redistribution in the ASE can be attributed to two processes – changes in surface mass balance (SMB) and dynamic thinning (Shepherd et al., 2019). Generally dynamic thinning involves the redistribution of ice that has a greater density than the material transported via SMB processes (Schröder et al., 2019). When generating estimates of mass change, these variations in density must be accounted for. We converted dh/dt grids to mass change grids by multiplying each grid cell by a defined density value, identified by application of a velocity threshold of 55 m/yr (Schröder et al., 2019) extracted from a long term ice surface velocity dataset (Mouginot et al., 2012; Rignot et al., 2011). Locations with velocities above this threshold were assigned a density of ice (917 kg/m^3) and locations with slower velocities were assigned the lower density of 550 kg/m^3 (McMillan et al., 2014; Riva et al., 2009; Schröder et al., 2019). We did not use surface change models such as the IMAU Firn Densification Model (Ligtenberg et al., 2011) or Community Firn Model (Stevens et al., 2020) to convert to mass since their coarse resolution results in the removal of short spatial wavelength surface change patterns. We calculate two additional density scenarios (provided in the Supporting Information) where all elevation changes are attributed to either ice or snow. We observe consistent

171 resolution dependent effects across every scenario and therefore focus on presenting our
172 velocity threshold solution for the remainder of the manuscript.
173
174 2.3 Elastic Modeling
175
176 Elastic parameter profiles were compiled using solid Earth models specific to Antarctica.
177 For the mantle we used the ANT-20 tomographic model (Lloyd et al., 2020) to extract Vs
178 (s wave velocity) and Vp (p wave velocity) and estimated mantle density from Pappa et
179 al. (2019). For regions in the mantle that are deeper than regions represented in the Lloyd
180 et al. (2020) and Pappa et al. (2019) models we used values from the Preliminary
181 Reference Earth Model (PREM) (Dziewonski & Anderson, 1981). Vs for the crustal
182 layers was extracted from the surface wave model of Zhou et al. (2022). Crustal Vp and
183 density were then estimated from the crustal Vs using the empirical relations of Brocher
184 (2005). These datasets were sampled onto a common grid using the H3 grid system at the
185 R3 resolution which is approximately equal to 1 degree (Brodsky, 2018). Load Love
186 number solutions to the equations of motion were calculated using the open source giapy
187 package (Kachuck, 2017) from the core-mantle boundary to the Earth surface (Durkin et
188 al., 2019). We used a harmonic order of 250,000, appropriate for modeling elastic
189 deformation with cell radii down to 160 m, to prevent truncation errors in the Green's
190 Functions (Bevis et al., 2016). Using higher harmonic orders did not result in significant
191 variations in our modeling estimates and decreases computational efficiency (see
192 Supporting Information). We repeated this procedure for 1000 randomly selected elastic
193 parameter profiles. Green's function computations and convolution of cell loads in the
194 space-domain were performed using the Regional ElAstic Rebound Calculator (REAR)
195 (Melini et al., 2018) and load Love numbers computed from the giapy algorithm
196 (Kachuck, 2017; Melini et al., 2018). From our 1000 runs we calculated the average and
197 standard deviation of the output elastic deformation rates to account for uncertainties
198 resulting from the use of a 1D earth model (Adhikari et al., 2021; Durkin et al., 2019).
199 We repeated this modeling procedure, resampling the high resolution surface change
200 solution at four different grid resolutions (6 km, 2.27 km, 0.86 km, and 0.32 km) whereby

distances correspond to the length (or diameter) of a square cell with the same area as the corresponding hexagon size (Brodsky, 2018).

2.5 Location Sensitivity Experiments

We test for the importance of the distance between surface load change and location of measurement within an elastic model by generating elastic deformation profiles at our four differing grid resolutions. Previous studies have shown that the greater the distance between the two the lower the recorded deformation (Wahr et al., 2013). However, how the magnitude and pattern of this decay varies with grid resolutions below 1 km remained unclear. We conduct these experiments by calculating vertical modeled elastic uplift at a fixed origin point as a surface loading disc is moved increasing distances away. As the cell is moved outwards from the origin by 1/3 of its radius, deformation at the origin is recorded until the cell is 10 degrees away from the origin location, producing a deformation profile. We repeat this experiment using cell diameters of 6, 2.27, 0.86 and 0.32 km (equal to those used when calculating elastic deformation at our GNSS sites). To ensure we are isolating the effects of grid resolution, the mass of the cell used remains constant for each resolution experiment.

2.6 GNSS Solutions

ANET-POLENET data was processed within a global network composed of ~2500 stations (using data spanning 1993 – 2022) using a parallelized Python wrapper for GAMIT/GLOBK v10.71 (Gómez et al., 2023). Atmospheric delays are estimated using the Vienna Mapping Functions (Boehm et al., 2006), and the effect of ocean tides accounted for by use of the FES2014b model (Lyard et al., 2021). An automated procedure was used to fit trajectory models to the displacement timeseries of each GNSS station (Bevis & Brown, 2014; Bevis et al., 2019). Seasonal displacement cycles are modeled using a 4-term Fourier series and the approach of Bevis et al. (2019) utilized to model deformation transients. Reference frame realization and trajectory modeling is implemented simultaneously to ensure internal geometrical consistency (Bevis & Brown,

2014). Many stations located along the Amundsen Sea coast have timeseries that contain artifacts related to antenna and radome icing. We mitigate these large and highly systematic errors by conducting a customized analysis, remodeling the timeseries and fine-tuning the trajectory models (Table S2). For more detailed information regarding GNSS processing please see Supporting Information.

3 Results

3.1 Elastic Deformation

We focus on the vertical component of elastic deformation, which is used as the primary calibration metric for GIA models and shows the greatest variation in magnitude when varying grid resolution. Horizontal components are provided in the Supporting Information. Modeled vertical elastic deformation rates at each GNSS site are provided for the four surface load grid resolution solutions (Table 1). We observe sub-millimeter variations in elastic response when using input surface load grids with between 0.32 and 6 km resolution (Figure 2). At four GNSS sites - TOMO, BERP, SLTR, and INMN - the spread in vertical elastic motion is statistically insignificant as the variation falls within the error bounds of our elastic solutions (Figure 2). Of the four remaining sites the location with the greatest spread is Martin Peninsula (MRTP), where the solution varies by 0.41 ± 0.36 mm/yr. Our average elastic solutions (RAv_e) for each site fall within 2

mm/yr of previously published solutions for GNSS sites in the region (Table 1) (Barletta et al. 2018; Caron et al. 2018).

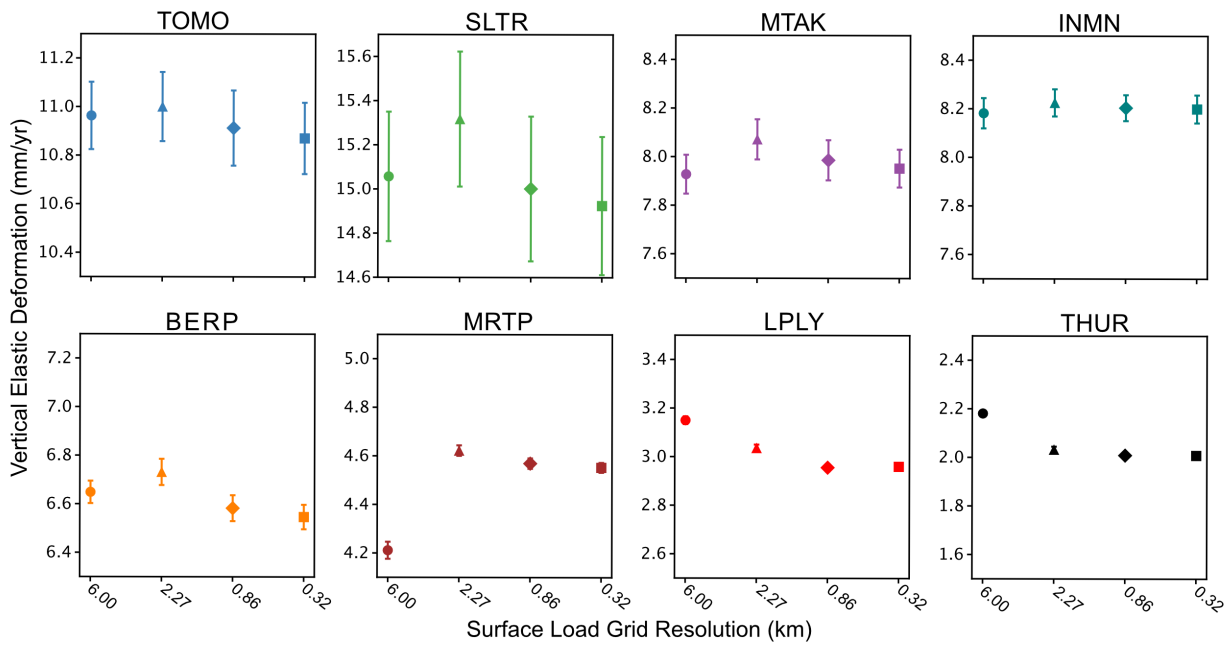

Figure 2. Vertical elastic deformation modeled at each GNSS site for each surface load grid resolution used within our elastic model. Uncertainty bounds are calculated from the standard deviation of the 1000 elastic model runs to account for the uncertainties associated with the use of a 1D earth profile.

Table 1. Vertical elastic deformation estimates and uncertainties for each grid resolution R6 (6 km), R7 (2.27 km), R8 (0.86 km), R9 (0.32 km), and elastic estimates from Barletta et al. (2018) (B_e) and Caron et al. (2018) (C_e). Updated GNSS vertical velocity solutions are provided and residual vertical velocities calculated by removing the average elastic uplift value (R_{Ave}).

	TOMO	BERP	SLTR	MTAK	MRTP	INMN	THUR	LPLY
$R6_e$ [mm/yr]	10.96 ± 0.14	6.65 ± 0.05	15.06 ± 0.29	7.93 ± 0.08	4.21 ± 0.04	8.18 ± 0.06	2.18 ± 0.01	3.15 ± 0.02
$R7_e$ [mm/yr]	11.00 ± 0.14	6.73 ± 0.05	15.32 ± 0.31	8.07 ± 0.08	4.62 ± 0.02	8.22 ± 0.06	2.03 ± 0.01	3.04 ± 0.01
$R8_e$ [mm/yr]	10.91 ± 0.15	6.58 ± 0.05	15.00 ± 0.33	7.99 ± 0.08	4.57 ± 0.02	8.20 ± 0.05	2.01 ± 0.01	2.96 ± 0.01
$R9_e$ [mm/yr]	10.87 ± 0.15	6.55 ± 0.05	14.92 ± 0.31	7.95 ± 0.08	4.55 ± 0.02	8.20 ± 0.06	2.01 ± 0.01	2.96 ± 0.01
RAv_e [mm/yr]	10.94 ± 0.15	6.63 ± 0.05	15.08 ± 0.31	7.98 ± 0.08	4.49 ± 0.02	8.20 ± 0.06	2.06 ± 0.01	3.03 ± 0.01
B_e [mm/yr]	10.7 ± 3.00	6.48 ± 0.7				9.15 ± 2.4	1.79 + 0.8	0.26 ± 0.5
C_e [mm/yr]	12.03	6.46					2.65	4.11
GNSS Uplift Rate [mm/yr]	59.49 ± 0.46	26.67 ± 0.12	49.65 ± 1.00	43.94 ± 0.89	14.12 ± 0.57	31.81 ± 0.38	-2.86 ± 0.11	5.24 ± 0.30
GNSS Residual [mm/yr]	48.55 ± 0.61	20.04 ± 0.17	34.57 ± 1.31	35.96 ± 0.97	9.63 ± 0.59	23.61 ± 0.44	-4.92 ± 0.12	2.21 ± 0.31

265

266 ### 3.2 GNSS Viscoelastic Residuals

267 We use our modeled average vertical elastic deformation rates (RAv_e) with our updated
268 GNSS solutions to calculate new GNSS residual estimates representing mantle-driven
269 viscoelastic GIA velocities. Vertical GNSS residuals are in excess of 20 mm/yr at five
270 GNSS stations, with the greatest rates located at the TOMO and MTAK (48.55 ± 0.61
271 mm/yr and 35.96 ± 0.97 mm/yr respectively. We derive the first residual vertical motion
272 values for 3 sites, of 34.57 ± 1.31 mm/yr (SLTR), 9.63 ± 0.59 mm/yr (MRTP) and 35.96
273 ± 0.97 mm/yr (MTAK). These high values are consistent with the model inference of
274 low viscosity mantle in the ASE region (Barletta et al., 2018).

275 ### 3.3 Location Sensitivity Experiments

276 Our location sensitivity experiments (detailed in section 2.5) show that there is a large
277 spread in modeled vertical elastic motion when loading discs of varying diameters are
278 close to the origin point (Figure 3). When the centroid of a 6 km diameter load cell is
279 placed at the origin, the modeled response at the origin is - 0.4 mm. We observe elastic
280 displacement over 30 times greater when repeating this experiment using a loading disc
281 of the same volume but with a cell diameter of 0.86 km (-16.33 mm). When the location
282 of the loading cell is moved away from the origin point the effects of disc diameter

283 decrease, before disappearing completely by ~ 5 km (Figure 3). We refer to this
284 approximate 5 km radius around the origin as the 'Zone of Sensitivity'.

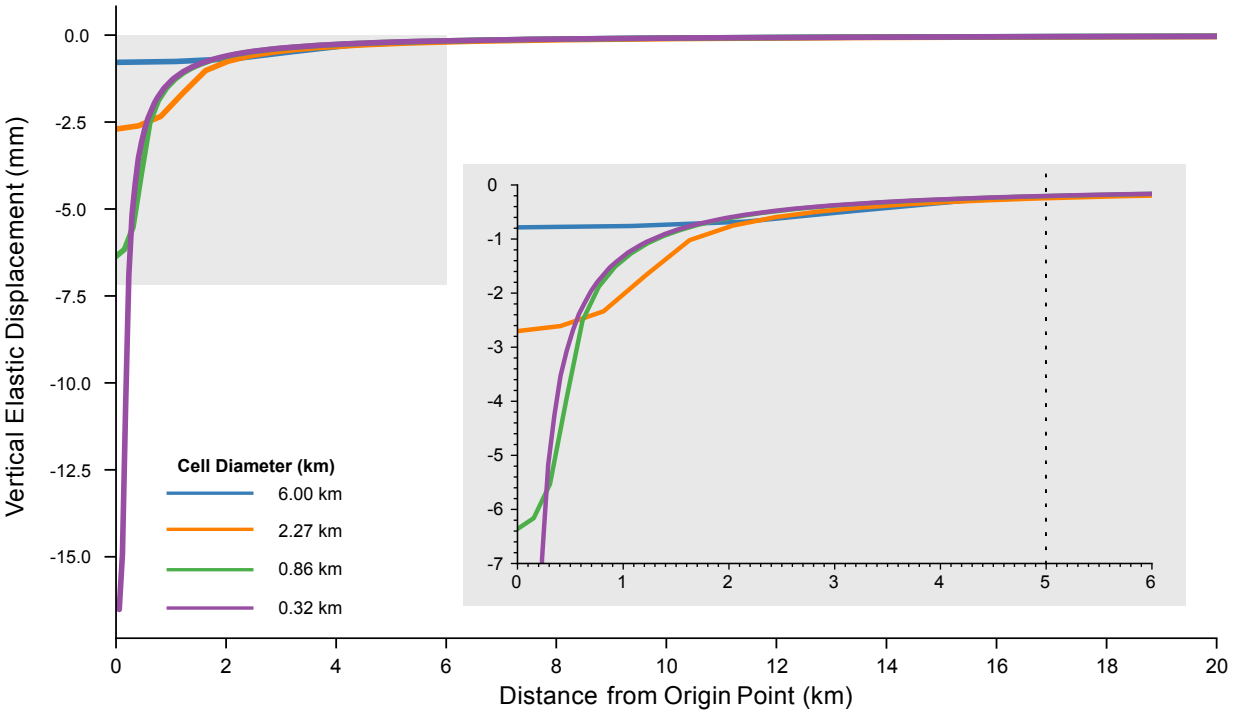

285

286

287 **Figure 3.** Profiles of vertical elastic deformation produced at each of the four surface load grid
288 resolutions generated by placing a load cell of fixed mass at increasing distance away from an
289 origin point. Inset graph provides an enlargement to better visualize variation in elastic
290 deformation occurring close to the origin point. The black dashed line shows the 5 km 'Zone of
291 Sensitivity' boundary.

292

293 **4 Discussion**

294 Sub-millimeter variations in modeled vertical elastic motion are observed when varying surface
295 grid resolutions between 0.32 and 6 km at GNSS sites within our study. At many sites these
296 variations fall within the error bounds of the elastic solutions, suggesting surface load grid
297 resolution is not strongly impacting modeled elastic estimates (Table 1). As a result of these
298 findings we suggest that ice dh/dt grid resolutions in excess of 6 km are presently sufficient for
299 modeling elastic deformation at GNSS sites in the ASE. Therefore, previously estimated ANET-

POLENT GNSS viscoelastic residuals, such as those of Barletta et al. (2018), are suitable to calibrate GIA model solutions and account for solid Earth motion in GRACE and GRACE-FO estimates of ice mass loss (Tapley et al., 2019; Velicogna et al., 2020).

This lack of variation when changing surface load grid resolution can be explained by the results of our location sensitivity experiments that show the decreasing influence of surface load grid resolution beyond 5 km from an origin point, or observation location. Isolating surface height changes (dh/dt) within this 'Zone of Sensitivity' at each GNSS site reveals that change rates are on average less than 1 m/yr. Intersecting this radius with our velocity threshold mask (Section x.x) shows that these changes are predominantly driven by SMB variations as opposed to dynamic thinning. Two GNSS sites within our study (INMN and SLTR) are situated near the grounding zone of major outlet glaciers where the greatest rates of grounded ice mass loss are observed (Bamber & Dawson, 2020; Milillo et al., 2022). INMN, near Pine Island Glacier, has been previously identified as being at risk for surface load grid resolution effects (Bamber & Dawson, 2020). We suggest that INMN is not presently at risk because the margin of Pine Island Glacier is located far outside of the sites 'Zone of Sensitivity'. This is also the case for SLTR that, although adjacent to the Kohler Glacier, is still situated farther than 5 km away from the glacier margin (Figure 1). Ice mass loss patterns within the ASE are evolving rapidly (Bamber & Dawson, 2020; Milillo et al., 2022), a trend that is predicted to continue. We therefore suggest it will be necessary to regularly re-evaluate the magnitude of mass changes within the 'Zone of Sensitivity' of INMN and SLTR, as well as those situated in the upper portion of glacier catchments such as TOMO and MRTP. This re-evaluation will be particularly important when modeling over extended temporal scales where ice mass loss patterns can evolve extensively through the modeling period (Larour et al., 2019)

Although our study is primarily focused on assessing uncertainties at ANET-POLENET ASE GNSS sites we suggest that the 'Zone of Sensitivity' concept may be a valuable tool when assessing the accuracy of gridded vertical elastic motion estimates, such as those used to correct dh/dt estimates (Smith et al., 2020). In these grids elastic deformation is calculated at many locations that would be affected by surface load change grid resolution, such as glacier margins and grounding zones where large surface changes fall within 5 km introducing unknown levels

of uncertainty. Furthermore, due to strong spatial control of surface load change grid resolution it may be possible to appropriately model gridded elastic deformation using a mixed resolution grid significantly improving computational speeds of large modeling frameworks

5 Conclusions

In this study we show that high resolution surface load change grids are not required to appropriately model vertical elastic deformation at current ANET-POLENET GNSS sites in the Amundsen Sea Embayment. Varying surface mass change grid resolutions down to 0.32 km resulted in vertical deformation variations of less than 0.5 mm/yr, with the values even smaller in the horizontal component. This small variation is explained by the relatively large spatial distances between the GNSS sites and the locations of major surface load changes, as demonstrated here by elastic deformation profiles that define a 'Zone of Sensitivity' of approximately 5 km surrounding a fixed location. Within this zone it is necessary to model the elastic response using high resolution surface mass load change grids. All current ANET-POLENT GNSS sites in the ASE region are located more than 5 km away from presently dominant changes in mass, and therefore are not sensitive to surface load change grid resolution solutions below 6 km in resolution. In contrast, the effects of surface load grid resolution are shown to be important at localities with high magnitude surface gradient changes occurring within 5 km. The results of this study and the identification of the 5 km 'Zone of Sensitivity' provide a potential framework to assess the uncertainty introduced by surface load grid resolution within elastic models and guide the creation of mixed resolution surface load change grids.

Acknowledgments

The authors declare that there are no conflicts of interest. This work was supported by NSF award numbers 0632322, 1249631, and 1745074 to the Ohio State University. Jasmine S. Hansen was supported by NASA Future Investigators in Earth Science grant 80NSSC20K1637. William J. Durkin was supported by the Byrd Postdoctoral Fellowship and NSF award 1745074. Geodetic data processing and trajectory analysis was completed at the Ohio State University by Michael Bevis, Demián Gómez, Eric Kendrick and David Saddler. We would also like to thank Stephanie Konfal and Whyjay Zheng for their assistance with this project.

Open Research

REMA data was provided by the Byrd Polar and Climate Research Center and the Polar Geospatial Center under NSF-OPP awards 1543501, 1810976, 1542736, 1559691, 1043681, 1541332, 0753663, 1548562, 1238993 and NASA award NNX10AN61G. Computer time provided through a Blue Waters Innovation Initiative. DEMs produced using data from Maxar DigitalGlobe, Inc. Altimtery data from Schröder et al. (2019) is available on PANGAEA (https://doi.org/10.1594/PANGAEA.897390). Ice velocity data is available at the National Snow and Ice Data Center (NSIDC) (https://nsidc.org/data/NSIDC-0484/versions/2) and surface elevation change from Smith et al. (2020). To process our DEM timeseries we used DEMCOREG (https://github.com/dshean/demcoreg), NASA Ames Stereo Pipeline (https://ti.arc.nasa.gov/tech/asr/groups/intelligent-robotics/ngt/stereo/), CARST (http://doi.org/10.5281/zenodo.3475693), and H3 (https://github.com/uber/h3). To calculate elastic deformation we use the packages giapy (Kachuck, 2017) and REAR (Melini et al., 2014) which are available at http://hpc.rm.ingv.it/rear/ and https://github.com/skachuck/giapy. Elastic deformation data from Caron et al. (2018) was provided upon request by L. Caron & S. Adhikari. GNSS solutions were processed by The Ohio State University from RINEX data available from UNAVCO (https://data.unavco.org/archive/gnss/rinex/obs.) and using Parallel.GAMIT (https://github.com/demiangomez/Parallel.GAMIT). Code to build surface change grids and output elastic deformation results can be found at https://github.com/jaha2600/ase_elastic_grl_2023/. Surface change grids and elastic model results are available at https://doi.org/10.5281/zenodo.7658864

References

Adhikari, S., Milne, G. A., Caron, L., Khan, S. A., Kjeldsen, K. K., Nilsson, J., et al. (2021). Decadal to Centennial Timescale Mantle Viscosity Inferred from Modern Crustal Uplift Rates in Greenland. *Geophysical Research Letters*, *48*(19), https://doi.org/10.1029/2021gl094040

Bamber, J. L., Oppenheimer, M., Kopp, R. E., Aspinall, W. P., & Cooke, R. M. (2019). Ice sheet contributions to future sea-level rise from structured expert judgment. *Proceedings of the National Academy of Sciences*, *116*(23), 11195-11200. https://doi.org/10.1073/pnas.1817205116

Bamber, J. L., & Dawson, G. J. (2020). Complex evolving patterns of mass loss from Antarctica's largest glacier. *Nature Geoscience*, *13*(2), 127–131. https://doi.org/10.1038/s*41*561-019-0527-z

Barletta, V. R., Bevis, M., Smith, B. E., Wilson, T., Brown, A., Bordoni, A., et al. (2018). Observed rapid bedrock uplift in Amundsen Sea Embayment promotes ice-sheet stability. *Science*, *360*(6395), 1335–1339. https://doi.org/10.1126/science.aao1*447*

Bevis M., Brown, A., & Kendrick, E. (2013). Devising stable geometrical reference frames for use in geodetic studies of vertical crustal motion, *Journal of Geodesy,* 87, 311-321, https://doi.org/10.1007/s00190-012-0600-5.

Bevis, M., & Brown, A. (2014). Trajectory models and reference frames for crustal motion geodesy, *Journal of Geodesy*, 88, 283-311. https://doi.org/10.1007/s00190-013-0685-5

Bevis, M., Melini, D., & Spada, G. (2016). On computing the geoelastic response to a disk load. *Geophysical Journal International*, *205*(3), 1804–1812. https://doi.org/10.1093/gji/ggw115

Bevis, M., Bedford, J., & Caccamise II, D. (2019). The art and science of trajectory modeling. In J-P. Montillet, M. Bos (Eds.), *Geodetic Time Series Analysis in Earth Sciences* (pp. 1-28) https://doi.org/10.1007/978-3-030-21718-1_1.

Boehm, J., Niell, A., Tregoning, P., & Schuh, H. (2006). Global Mapping Function (GMF): A new empirical mapping function based on numerical weather model data. *Geophysical Research Letters, 33*(7), https://doi.org/10.1029/2005GL025546

Brocher, T. M. (2005). Empirical Relations between Elastic Wavespeeds and Density in the Earth's Crust. *Bulletin of the Seismological Society of America*, *95*(6), 2081–2092. https://doi.org/10.1785/0120050077

Caron, L., Ivins, E. R., Larour, E., Adhikari, S., Nilsson, J., & Blewitt, G. (2018). GIA Model Statistics for GRACE Hydrology, Cryosphere, and Ocean Science. *Geophysical Research Letters*. *45*(5), 2203–2212. https://doi.org/10.1002/2017gl076644

Caron, Lambert, & Ivins, E. R. (2020). A baseline Antarctic GIA correction for space gravimetry. *Earth and Planetary Science Letters*, *531*. https://doi.org/10.1016/j.epsl.2019.115957

Coulon, V., Bulthuis, K., Whitehouse, P. L., Sun, S., Haubner, K., Zipf, L., & Pattyn, F. (2021). Contrasting Response of West and East Antarctic Ice Sheets to Glacial Isostatic Adjustment. *Journal of Geophysical Research: Earth Surface*, *126*(7). https://doi.org/10.1029/2020jf006003

Dai, C., & Howat, I. M. (2017). Measuring Lava Flows With ArcticDEM: Application to the 2012–2013 Eruption of Tolbachik, Kamchatka. *Geophysical Research Letters, 44*(24), 133-140. https://doi.org/10.1002/2017gl075920

Durkin, W., Kachuck, S., & Pritchard, M. (2019). The Importance of the Inelastic and Elastic Structures of the Crust in Constraining Glacial Density, Mass Change, and Isostatic Adjustment From Geodetic Observations in Southeast Alaska. *Journal of Geophysical Research: Solid Earth*, *126*(1), 1106-1119. https://doi.org/10.1029/2018jb016399

Dziewonski, A. M., & Anderson, D. L. (1981). Preliminary reference Earth model. *Physics of the Earth and Planetary Interiors*, *25*(4), 297–356. https://doi.org/10.1016/0031-9201(81)90046-7

Gerrish, L., Fretwell, P., & Cooper, P. (2021). High resolution vector polylines of the Antarctic coastline (Version 7.4) [Dataset]. NERC EDS UK Polar Data Centre. https://doi.org/10.5285/e46be5bc-ef8e-4fd5-967b-92863fbe2835

Gómez, D. (2023). Parallel.GAMIT. [Software]. GitHub. https://github.com/demiangomez/Parallel.GAMIT

Gomez, N., Pollard, D., & Holland, D. (2015). Sea-level feedback lowers projections of future Antarctic Ice-Sheet mass loss. *Nature Communications*, 6. https://doi.org/*10*.1038/ncomms9798

Heeszel, D. S., Wiens, D. A., Anandakrishnan, S., Aster, R. C., Dalziel, I. W. D., Huerta, A. D., et al. (2016). Upper mantle structure of central and West Antarctica from array analysis of Rayleigh wave phase velocities. *Journal of Geophysical Research: Solid Earth*, *121*(3), 1758–1775. https://doi.org/10.1002/2015jb012616

Howat, I. M., Porter, C., Smith, B. E., Noh, M.-J., & Morin, P. (2019). The Reference Elevation Model of Antarctica. *The Cryosphere*, *13*(2), 665–674. https://doi.org/10.5194/tc-13-665-2019

Hughes, T. J. (1981). The weak underbelly of the West Antarctic ice sheet. *Journal of Glaciology*, *27*(97), 518–525. https://doi.org/10.3189/s002214300001159x

Kachuck, S. B. (2017). giapy: Glacial Isostatic Adjustment in Python (Version 1.0.0) [Software]. GitHub. https://github.com/skachuck/giapy

Kjeldsen, K. K., Khan, S. A., Colgan, W. T., MacGregor, J. A., & Fausto, R. S. (2020). Time-Varying Ice Sheet Mask: Implications on Ice-Sheet Mass Balance and Crustal Uplift. *Journal of Geophysical Research: Earth Surface*, *125*(12). https://doi.org/10.1029/2020jf005775

Larour, E., Seroussi, H., Adhikari, S., Ivins, E., Caron, L., Morlighem, M., & Schlegel, N. (2019). Slowdown in Antarctic mass loss from solid Earth and sea-level feedbacks. *Science, 364*(6444), eaav7908. https://doi.org/10.1126/science.aav7908

Ligtenberg, S. R. M., Helsen, M. M., & Broeke, M. R. van den. (2011). An improved semi-empirical model for the densification of Antarctic firn. *The Cryosphere, 5*(4), 809–819. https://doi.org/10.5194/tc-5-809-2011

Liu, L., Khan, S. A., Dam, T., Ma, J. H. Y., & Bevis, M. (2017). Annual variations in GPS-

483 measured vertical displacements near Upernavik Isstrøm (Greenland) and contributions from
484 surface mass loading. *Journal of Geophysical Research: Solid Earth, 122*(1), 677–691.
485 https://doi.org/10.1002/2016jb013494
486
487 Lloyd, A. J., Wiens, D. A., Zhu, H., Tromp, J., Nyblade, A. A., Aster, R. C., et al. (2020).
488 Seismic Structure of the Antarctic Upper Mantle Imaged with Adjoint Tomography. *Journal of*
489 *Geophysical Research: Solid Earth, 125*(3). https://doi.org/10.1029/2019jb017823
490
491 Lyard, F. H., Allain, D. J., Cancet, M., Carrère, L., & Picot, N. (2021). FES2014 global ocean
492 tides atlas: design and performances. *Ocean Science, 17*(3),1–40. https://doi.org/10.5194/os-17-
493 615-2021
494
495 Martín-Español, A., King, M. A., Zammit-Mangion, A., Andrews, S. B., Moore, P., & Bamber,
496 J. L. (2016a). An assessment of forward and inverse GIA solutions for Antarctica. *Journal of*
497 *Geophysical Research: Solid Earth, 121*(9), 6947–6965. https://doi.org/10.1002/2016jb013154
498
499 Martín-Español, A., Zammit-Mangion, A., Clarke, P. J., Flament, T., Helm, V., King, M. A., et
500 al. (2016b). Spatial and temporal Antarctic Ice Sheet mass trends, glacio-isostatic adjustment,
501 and surface processes from a joint inversion of satellite altimeter, gravity, and GPS data. *Journal*
502 *of Geophysical Research: Earth Surface, 121*(2), 182–200. https://doi.org/10.1002/2015jf003550
503
504 McMillan, M., Shepherd, A., Sundal, A., Briggs, K., Muir, A., Ridout, A., et al. (2014).
505 Increased ice losses from Antarctica detected by CryoSat-2. *Geophysical Research Letters,*
506 *41*(11), 3899–3905. https://doi.org/10.1002/2014gl060111
507
508 Melini, D., Spada, G., Gegout, P., King, M., & Consorzi, A. (2018). REAR - A Regional Elastic
509 Rebound Calculator. (Verson 1.0.1) [Software]. GitHub. http://github.com/danielemelini/rear
510
511 Melkonian, A.K. (2014). *Quantifying and Characterizing Mass Loss From Icefields Using*
512 *Remote Sensing* (Doctoral dissertation). Retrieved from Cornell eCommons.

(https://hdl.handle.net/1813/39298) Ithaca, NY: Cornell University.

Milillo, P., Rignot, E., Rizzoli, P., Scheuchl, B., Mouginot, J., Bueso-Bello, J. L., et al. (2022). Rapid glacier retreat rates observed in West Antarctica. *Nature Geoscience, 15*(1), 48–53. https://doi.org/10.1038/s41561-021-00877-z

Mouginot, J., Scheuchl, B., & Rignot, E. (2012). Mapping of Ice Motion in Antarctica Using Synthetic-Aperture Radar Data. *Remote Sensing*, *4*(9), 2753–2767. https://doi.org/10.3390/rs4092753

Nilsson, J., Gardner, A., Sørensen, L. S., & Forsberg, R. (2016). Improved retrieval of land ice topography from CryoSat-2 data and its impact for volume-change estimation of the Greenland Ice Sheet. *The Cryosphere, 10*(6), 2953–2969. https://doi.org/10.5194/tc-10-2953-2016

Noh, M.-J., & Howat, I. M. (2015). Automated stereo-photogrammetric DEM generation at high latitudes: Surface Extraction with TIN-based Search-space Minimization (SETSM) validation and demonstration over glaciated regions. *GIScience & Remote Sensing*, *52*(2), 198–217. https://doi.org/10.1080/15481603.2015.1008621

Pappa, F., Ebbing, J., Ferraccioli, F., & Wal, W. (2019). Modeling Satellite Gravity Gradient Data to Derive Density, Temperature, and Viscosity Structure of the Antarctic Lithosphere. *Journal of Geophysical Research: Solid Earth, 124*(11), 12053–12076. https://doi.org/10.1029/2019jb017997

Rignot, E., Mouginot, J., & Scheuchl, B. (2011). Ice Flow of the Antarctic Ice Sheet. *Science, 333*(6048), 1427–1430. https://doi.org/10.1126/science.1208336

Rignot, E., J. Mouginot, & Scheuchl, B. (2017). MEaSUREs InSAR-Based Antarctica Ice Velocity Map (Version 2). [Dataset] NASA National Snow and Ice Data Center Distributed Active Archive Center. https://doi.org/10.5067/D7GK8F5J8M8R.

Rignot, Eric, Mouginot, J., Scheuchl, B., Broeke, M. van den, Wessem, M. J. van, & Morlighem, M. (2019). Four decades of Antarctic Ice Sheet mass balance from 1979–2017. *Proceedings of the National Academy of Sciences, 116*(4), 201812883. https://doi.org/10.1073/pnas.1812883116

Riva, R. E. M., Gunter, B. C., Urban, T. J., Vermeersen, B. L. A., Lindenbergh, R. C., Helsen, M. M., et al. (2009). Glacial Isostatic Adjustment over Antarctica from combined ICESat and GRACE satellite data. *Earth and Planetary Science Letters, 288*(3–4), 516–523. https://doi.org/10.1016/j.epsl.2009.10.013

Schoof, C. (2007). Ice sheet grounding line dynamics: Steady states, stability, and hysteresis. *Journal of Geophysical Research: Earth Surface*, *112*(F3). https://doi.org/10.1029/2006jf000664

Schröder, L., Horwath, M., Dietrich, R., Helm, V., Broeke, M. R. van den, & Ligtenberg, S. R. M. (2019). Four decades of Antarctic surface elevation changes from multi-mission satellite altimetry. *The Cryosphere, 13*(2), 427–449. https://doi.org/10.5194/tc-13-427-2019

Schröder, L., Horwath, M., Dietrich, R., Helm, V., Broeke, M. R. van den, & Ligtenberg, S. R. M. (2019). Gridded surface elevation changes from multi-mission satellite altimetry 1978-2017 [Dataset]. PANGAEA. https://doi.org/10.1594/PANGAEA.897390

Shean, D. E., Alexandrov, O., Moratto, Z. M., Smith, B. E., Joughin, I. R., Porter, C., & Morin, P. (2016). An automated, open-source pipeline for mass production of digital elevation models (DEMs) from very-high-resolution commercial stereo satellite imagery. *ISPRS Journal of Photogrammetry and Remote Sensing*, 116, 101–117. https://doi.org/10.1016/j.isprsjprs.2016.03.012

Shean, D. E., Joughin, I. R., Dutrieux, P., Smith, B. E., & Berthier, E. (2019). Ice shelf basal melt rates from a high-resolution digital elevation model (DEM) record for Pine Island Glacier, Antarctica. *The Cryosphere, 13*(10), 2633–2656. https://doi.org/10.5194/tc-13-2633-2019

Shepherd, A., Gilbert, L., Muir, A. S., Konrad, H., McMillan, M., Slater, T., et al. (2019). Trends in Antarctic Ice Sheet Elevation and Mass. *Geophysical Research Letters, 46*(14), 8174–8183. https://doi.org/10.1029/2019gl082182

Smith, B., Fricker, H. A., Gardner, A. S., Medley, B., Nilsson, J., Paolo, F. S., et al. (2020). Pervasive ice sheet mass loss reflects competing ocean and atmosphere processes. *Science, 367*(6496), 1239-1242. https://doi.org/10.1126/science.aaz5845

Stevens, C. M., Verjans, V., Lundin, J. M. D., Kahle, E. C., Horlings, A. N., Horlings, B. I., & Waddington, E. D. (2020). The Community Firn Model (CFM) v1.0. *Geoscientific Model Development*, *13*(9), 4355–4377. https://doi.org/10.5194/gmd-13-4355-2020

Tapley, B. D., Watkins, M. M., Flechtner, F., Reigber, C., Bettadpur, S., Rodell, M., et al. (2019). Contributions of GRACE to understanding climate change. *Nature Climate Change*, *9*(5), 358–369. https://doi.org/10.1038/s41558-019-0456-2

Uber Technologies Inc. (2023). H3: Hexagonal hierarchical geospatial indexing system (Version 3.5.0). [Software]. GitHub. https://github.com/uber/h3

Velicogna, I., Mohajerani, Y., A, G., Landerer, F., Mouginot, J., Noel, B., et al. (2020). Continuity of Ice Sheet Mass Loss in Greenland and Antarctica From the GRACE and GRACE Follow-On Missions. *Geophysical Research Letters, 47*(8). https://doi.org/10.1029/2020gl087291

Wahr, J., Khan, S. A., Dam, T., Liu, L., Angelen, J. H., Broeke, M. R., & Meertens, C. M. (2013). The use of GPS horizontals for loading studies, with applications to northern California and southeast Greenland. *Journal of Geophysical Research: Solid Earth, 118*(4), 1795-1806. https://doi.org/10.1002/jgrb.50104

603 Wan, J. X. W., Gomez, N., Latychev, K., & Han, H. K. (2022). Resolving glacial isostatic
604 adjustment (GIA) in response to modern and future ice loss at marine grounding lines in West
605 Antarctica. *The Cryosphere*, *16*(6), 2203-2223. https://doi.org/10.5194/tc-16-2203-2022
606
607 Weertman, J. (1974). Stability of the Junction of an Ice Sheet and an Ice Shelf. *Journal of*
608 *Glaciology, 13*(67), 3–11. https://doi.org/10.3189/s0022143000023327
609
610 Zheng, W., Pritchard, M. E., Willis, M. J., Tepes, P., Gourmelen, N., Benham, T. J., &
611 Dowdeswell, J. A. (2018). Accelerating glacier mass loss on Franz Josef Land, Russian Arctic.
612 *Remote Sensing of Environment*, 211, 357–375. https://doi.org/10.1016/j.rse.2018.04.004
613
614 Zheng, W., Durkin, W. J., Melkonian, A. K., & Pritchard, M. E. (2019). Cryosphere And Remote
615 Sensing Toolkit (CARST) v1.0.1 (Version v1.0.1) [Software]. Zenodo.
616 https://doi.org/10.5281/zenodo.3475693
617
618 Zhou, Z., Wiens, D. A., Shen, W., Aster, R. C., Nyblade, A., & Wilson, T. J. (2022). Radial
619 Anisotropy and sediment thickness of West and Central Antarctica estimated from Rayleigh and
620 Love wave velocities. *Journal of Geophysical Research: Solid Earth*, *127*(3).
621 https://doi.org/10.1029/2021JB022857

Geophysical Research Letters

Supporting Information for

Sensitivity of Modeled Elastic Deformation in the Amundsen Sea Embayment

J. S. Hansen[1,2], W. J. Durkin[3], M. J. Willis[1,2,4], T. J. Wilson[3], M. G. Bevis[3], D. D. Gómez[3]

[1] Department of Geological Sciences, University of Colorado Boulder

[2] Cooperative Institute for Research in Environmental Sciences

[3] School of Earth Sciences, The Ohio State University

[4] Department of Geosciences, Virginia Tech

Contents of this file

Additional Supporting Information (Files uploaded separately)

Introduction

We provide further information regarding the production of high-resolution grids of surface change in West Antarctica, including information about coregistration and grid uncertainties. We also provide full elastic modeling results and uncertainties. Finally, we provide a detailed description of ANET-POLENET GNSS processing and maps of surface changes occurring within 5 km of ANET-POLENET GNSS sites.

Text S1. Dynamic Coregistration and Surface Change grid Uncertainties

As a result of the lack of bedrock outcrops across much of the ASE region suitable for static registration points, we identify additional locations suitable for coregistration of DEM strips from the Reference Elevation Model of Antarctica (REMA) (Howat et al.,

2019). We extract these coregistration points from an 8m DEM mosaic available as part of REMA that we filter by long term vertical and horizontal velocities (from the NASA MEaSUREs velocity product (Mouginot et al., 2012; Rignot et al., 2011) and ICESat-ICESat-2 long term record of surface change (Smith et al., 2020). The higher the allowable threshold applied to the vertical and horizontal datasets, the more reference points become available for coregistration. However, enabling coregistration over 'faster' moving locations may impact the quality of coregistration and subsequently calculations of surface elevation change (dh/dt). To check that the dynamic thresholds we use do not strongly influence dh/dt solutions, we use Google Earth Engine to create an array of masked DEM mosaic datasets for nine different vertical and horizontal velocity configurations (Table S1). We use vertical velocity values from the Smith et al. (2020) mosaic that vary between 0.1 - 0.5 m/yr, and use a 1 - 10 m/yr threshold for horizontal velocity from MEaSUREs (Rignot et al., 2017). Each of the 9 masked REMA mosaic datasets is then used as a reference point cloud to coregister our set of DEM strips, following the methods described in section 2.1 of the main text. This produces 9 sets of DEM strips that we use to create 9 different maps of surface elevation change (dh/dt) utilizing the CARST package (Zheng et al., 2018). We compare the different mean rates of surface change that each solution provides, for each GNSS site (Table S1). The maximum spread in mean surface change rate is found at SLTR (1.72 m/yr). The majority of sites see differences less than 1 m/yr which provides us with confidence that we can utilize our least strict point cloud definition of 0.5 m/yr vertical velocity, and 10 m/yr horizontal, without affecting the results of our dh/dt.

For our finalized dh/dt grids we output dh/dt uncertainty maps (Figure S1). Volume change uncertainties are calculated following the methods of Zheng et al. (2018) and Melkonian et al. (2014) where we classify measurements from the same stack of DEMs as being mutually independent. Measurements from different DEM stacks are treated as independent. We group uncertainties by DEM stack and calculate bulk uncertainty using equation 4. from Zheng et al. (2018). Uncertainty maps can be found in Figure S1. For the uncertainties of Schroder et al. (2019) grid we use the uncertainty estimates provided by Schröder et al. (2019), and an estimated correlation length of 100 km (Nilsson et al., 2016).

Text S2. Geodetic Data Processing with GAMIT/GLOBK

We processed the ANET GPS data within a global network composed of ~2500 stations (with data spanning from 1993 to 2022, ~4 million station-days) using a parallelized Python wrapper for GAMIT/GLOBK v10.71 (Gómez, 2023). Processing of GPS data used the orbits and antenna calibration parameters available from the International GNSS Service (IGS14 reference frame), the Vienna Mapping Functions (Boehm et al., 2006) to estimate the atmospheric delays, and the ocean tide loading model FES2014b (Lyard et al., 2021).

Text S3. Station Trajectory Analysis and Reference Frame Realization

We use an automated procedure to fit trajectory models to the displacement time series of each CGPS station (Bevis & Brown, 2014; Bevis et al., 2019). This model is composed of up to 4 sub-models: a displacement trend (nearly always linear in time), a series of 0, 1 or more steps or Heaviside jumps, a seasonal displacement cycle, and,

when needed, logarithmic transients that accommodate transient displacements. Most trend models invoke constant velocity, but some invoke quadratic or higher order trends in order to account for accelerating patterns of displacement. The time of the jumps are imposed by us, but the amplitudes of these jumps are estimated. These jumps allow the model to incorporate coseismic displacements, and also coordinate discontinuities driven by changes in geodetic station equipment (mostly changes of antennas or radomes). Seasonal displacement cycles are modeled using a 4-term Fourier series (with annual and semi-annual periods). Our approach to modeling post-seismic transients followed the approach of Bevis et al. (2019) rather than that of Bevis and Brown (2014).

Reference frame (RF) realization and trajectory modeling are implemented simultaneously, so as to ensure internal geometrical consistency (Bevis & Brown, 2014). The horizontal aspect of the RF, in velocity or rate space, is imposed by minimizing the RMS horizontal velocities of a set of stations referred to as HREF. These stations are nominally part of the rigid portions of the Antarctica plate, in which there are no relative velocities driven by tectonics. The vertical aspect of the RF in velocity space is that which minimizes the RMS vertical velocities of a global set of CGPS stations called VREF. This set is chosen using the "ensemble of RFs" approach described by Bevis et al. (2013). The 16 HREF stations are VESL, SYOG, MAW1, DAV1, ABOA, BURI, LWN0, WHN0, ZHON, NONS, BRIP, BELG, COTE, FLM5 and BUMS in the Antarctic continent, and KERG in Kerguelen Island. The RMS horizontal velocity of these stations in the final ANET frame is 0.29 mm/yr. The RMS vertical velocity of the 850 VREF stations is 0.92 mm/yr. The station displacement time series and best-fit trajectory models referred to this RF are denoted as the geodetic solution pg03f_PC_H16.

Text S4. Mitigation of Icing Noise: Fine-Tuning the Trajectory Models for the Amundsen Sea Region Stations

All the trajectory models in the solution pg03f_PC_H16 were computed using default assumptions regarding the nature of the positioning noise. But many of the stations located along or near the Amundsen Sea Coast have time series containing highly structured and high amplitude artifacts driven by rime icing of the antenna and its radome and/or by invasion of the interior of the radome by fine ice crystals. Mitigating these large and highly systematic errors requires a customized analysis in which we remodel the time series making a range of decisions about the time window selected for modeling, which daily coordinate solutions are downweighted within this window because they are designated as outliers, and how the trajectory model is formulated. In adjusting the trajectory model we reconsider estimation of any displacement cycle, if a 4-term or a 2-term Fourier series should be used, and examine linear and quadratic trend models, keeping in mind that icing noise can produce much larger perturbations of a quadratic model relative to a time-linear trend model. We perform a range of experiments for each station, designate selected solutions as acceptable and identify a preferred solution, based on an a posteriori inspection of the results, the WRMS misfit, amongst other metrics. The formal standard errors for the preferred velocity estimates are adjusted upwards, if necessary, to accommodate the range of the velocity estimates in the other acceptable solutions.

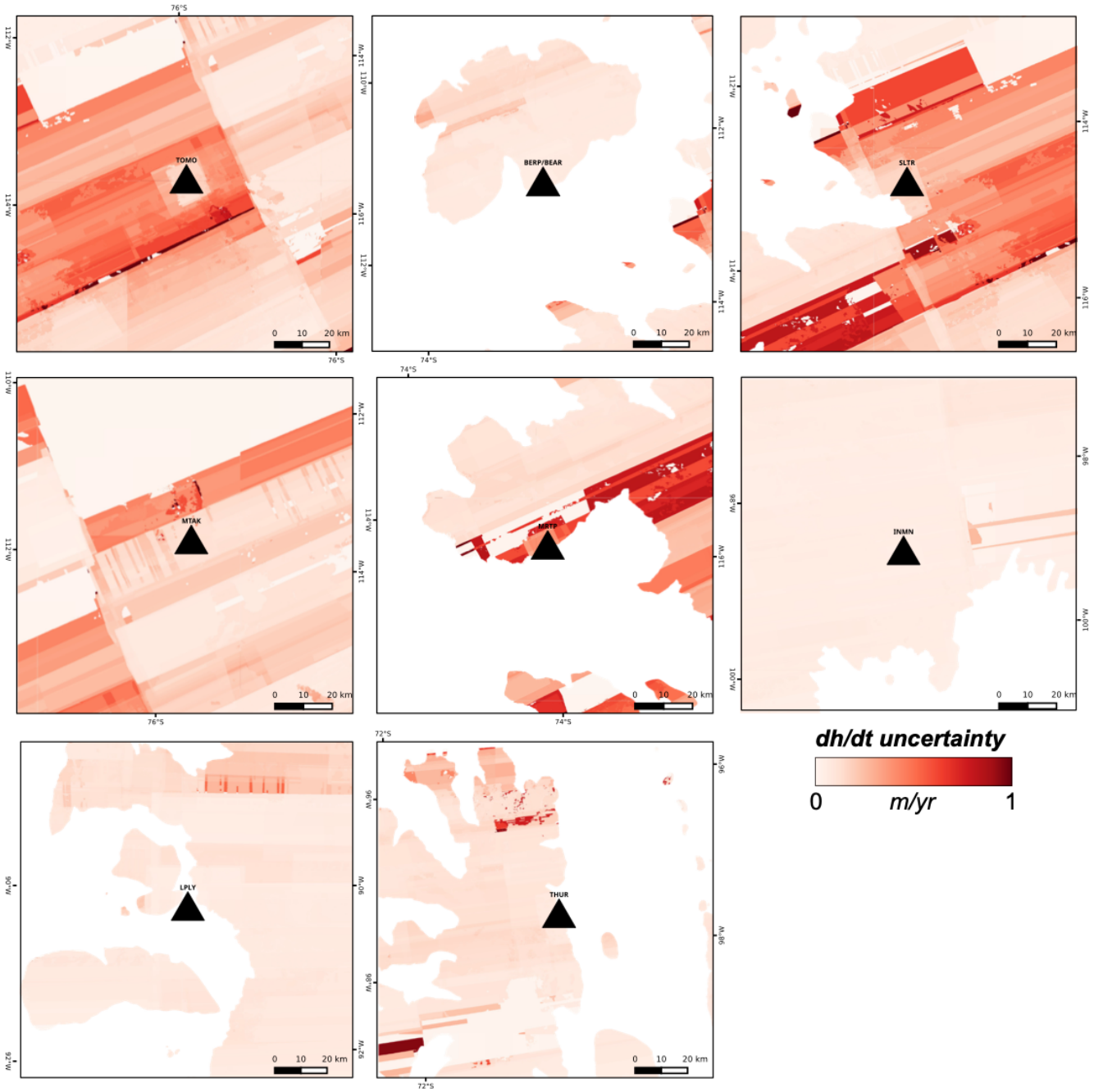

Figure S1. Grids of surface elevation change uncertainty produced at each GNSS site region following the methods of Zheng et al. (2018). Darker red regions have a greater associated uncertainty.

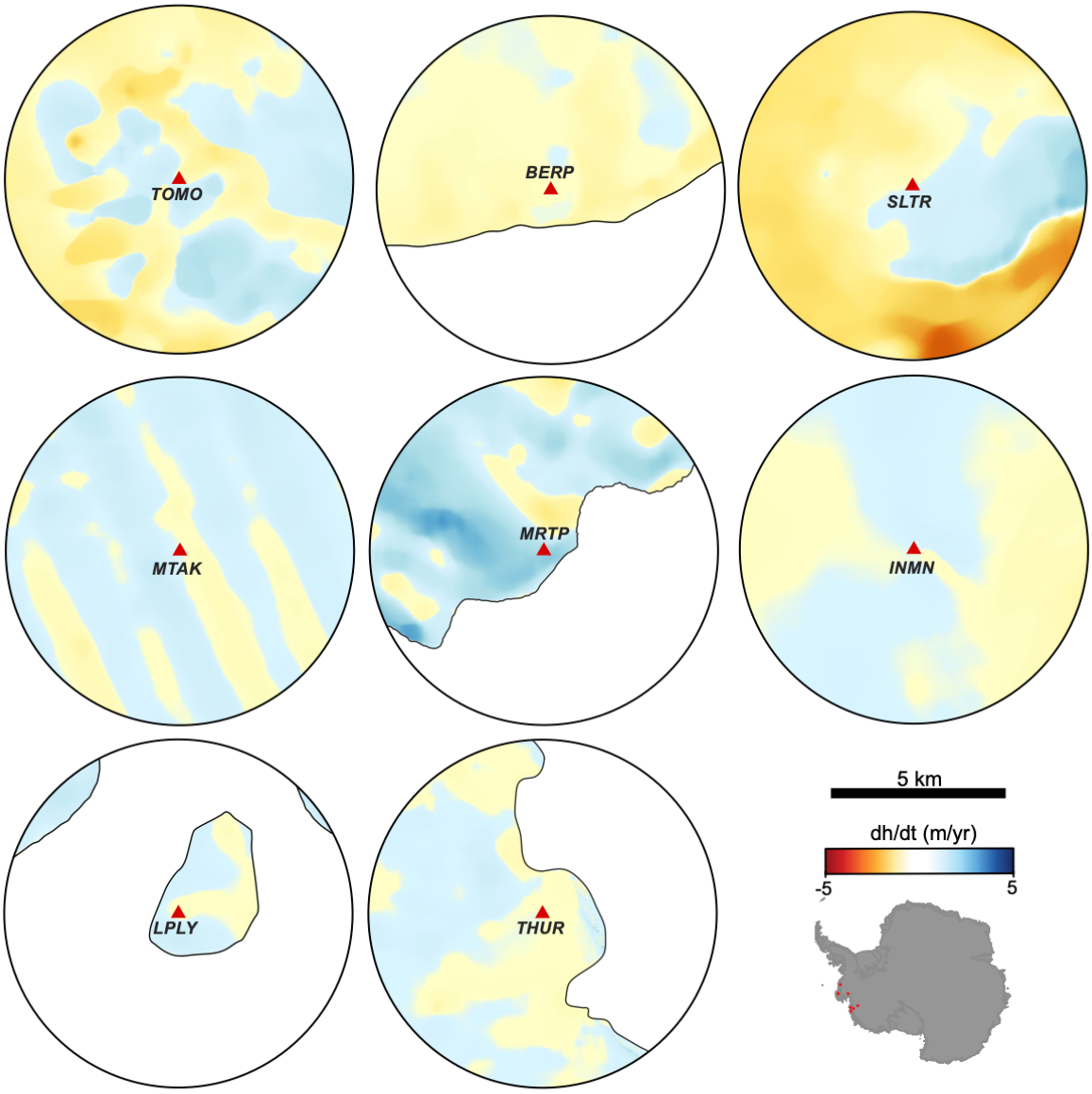

Figure S2. Surface elevation change (dh/dt) maps around each of the eight GNSS sites located in the Amundsen Sea Embayment Region. A 5 km radius around each site is marked on the figure to indicate the distance threshold outside of which there is a greatly reduced sensitivity to the resolution of your surface load change grid.

Table S1. Surface elevation change grids produced using DEM stacks coregistered to different dynamic point thresholds. For more information refer to Text S1.

Vertical velocity threshold (m/yr)		0.5	0.5	0.5	0.25	0.25	0.25	0.1	0.1	0.1	SPREAD (m/yr)
Horizontal velocity threshold (m/yr)		1	5	10	5	1	10	5	1	10	
mean dh/dt (m/yr)	BERP	-0.38	-0.38	-0.32	-0.12	-0.54	-0.11	-0.40	-0.45	-0.40	**0.54**
	INMN	-0.51	-0.49	-0.46	-0.26	-0.50	0.07	-0.51	-0.50	-0.50	**0.51**
	LPLY	-0.15	-0.15	-0.16	-0.71	-0.15	-0.51	-0.14	-0.16	-0.14	**0.71**
	MRTP	-0.15	0.00	0.09	-0.60	-0.36	0.41	-0.16	-0.44	-0.21	**0.60**
	MTAK	-0.15	0.00	0.09	-0.60	-0.36	0.41	-0.16	-0.44	-0.21	**0.60**
	SLTR	-1.63	-1.48	-1.65	0.00	-1.69	-0.20	-1.69	-1.72	-1.65	1.72
	THUR	0.08	0.05	0.04	0.46	0.08	0.38	0.05	0.07	0.04	0.04
	TOMO	-1.05	-0.97	-1.01	-0.39	-1.10	-0.45	-1.12	-1.19	-1.12	**1.19**

Table S2. GNSS solutions

Station	Vu	Su	Ve	Se	Vn	Sn
IGS_BERP	26.67	0.12	1.22	0.06	9.43	0.05
IGS_INMN	31.81	0.38	-2.55	0.2	7.22	0.21
IGS_LPLY	5.24	0.3	-1.07	0.19	-0.19	0.16
IGS_MRTP	14.12	0.57	0.4	0.2	4.17	0.16
IGS_MTAK	43.94	0.89	-2.38	0.21	-7.64	0.2
IGS_SLTR	49.65	1	-3.23	0.21	10.8	0.2
IGS_THUR	-2.86	0.11	-1.32	0.06	-2.63	0.06
IGS_TOMO	50.49	0.46	-5.86	0.16	-2.74	0.2

Caption for Table S3. Elastic modeling results for each directional component at each GNSS site for each surface load grid resolution and the three density scenarios.

Uncertainties are provided that capture the variability from 1000 model runs using a randomly sampled 1D elastic profile.

References

Bevis M., Brown, A., & Kendrick, E. (2013). Devising stable geometrical reference frames for use in geodetic studies of vertical crustal motion, *Journal of Geodesy,* 87, 311-321, https://doi.org/10.1007/s00190-012-0600-5.

Bevis, M., & Brown, A. (2014). Trajectory models and reference frames for crustal motion geodesy, *Journal of Geodesy,* 88, 283-311, https://doi.org/10.1007/s00190-013-0685-5.

Bevis, M., Bedford, J., & Caccamise II, D. (2019). The art and science of trajectory modeling. In J-P. Montillet, M. Bos (Eds.) *Geodetic Time Series Analysis in Earth Sciences* (pp. 1-28) https://doi.org/10.1007/978-3-030-21718-1_1.

Boehm, J., Niell, A., Tregoning, P., & Schuh, H. (2006). Global Mapping Function (GMF): A new empirical mapping function based on numerical weather model data. *Geophysical Research Letters, 33*(7), L07304. https://doi.org/10.1029/2005GL025546

Gómez, D. (2023*)* Parallel.GAMIT. [Software]. GitHub. https://github.com/demiangomez/Parallel.GAMIT

Howat, I. M., Porter, C., Smith, B. E., Noh, M.-J., & Morin, P. (2019). The Reference Elevation Model of Antarctica. *The Cryosphere, 13*(2), 665–674. https://doi.org/10.5194/tc-13-665-2019

Hughes, T. J. (1981). The weak underbelly of the West Antarctic ice sheet. *Journal of Glaciology, 27*(97), 518–525. https://doi.org/10.3189/s002214300001159x

Lyard, F. H., Allain, D. J., Cancet, M., Carrère, L., & Picot, N. (2021). FES2014 global ocean tides atlas: design and performances. *Ocean Science Discussions*, *17*(3),1–40. https://doi.org/10.5194/os-17-615-2021

Melkonian, A.K. (2014). *Quantifying and Characterizing Mass Loss From Icefields Using Remote Sensing* (Doctoral Dissertation). Retrieved from Cornell eCommons. (https://hdl.handle.net/1813/39298) Ithaca, NY: Cornell University.

Mouginot, J., Scheuchl, B., & Rignot, E. (2012). Mapping of Ice Motion in Antarctica Using Synthetic-Aperture Radar Data. *Remote Sensing, 4*(9), 2753–2767. https://doi.org/10.3390/rs4092753

Nilsson, J., Gardner, A., Sørensen, L. S., & Forsberg, R. (2016). Improved retrieval of land ice topography from CryoSat-2 data and its impact for volume-change

estimation of the Greenland Ice Sheet. *The Cryosphere, 10*(6), 2953–2969. https://doi.org/10.5194/tc-10-2953-2016

Rignot, E., Mouginot, J., & Scheuchl, B. (2011). Ice Flow of the Antarctic Ice Sheet. *Science, 333*(6048), 1427–1430. https://doi.org/10.1126/science.1208336

Rignot, E., Mouginot, J., & Scheuchl, B. (2017). MEaSUREs InSAR-Based Antarctica Ice Velocity Map (Version 2). [Dataset] NASA National Snow and Ice Data Center Distributed Active Archive Center. https://doi.org/10.5067/D7GK8F5J8M8R

Schröder, L., Horwath, M., Dietrich, R., Helm, V., Broeke, M. R. van den, & Ligtenberg, S. R. M. (2019). Four decades of Antarctic surface elevation changes from multi-mission satellite altimetry. *The Cryosphere, 13*(2), 427–449. https://doi.org/10.5194/tc-13-427-2019

Smith, B., Fricker, H. A., Gardner, A. S., Medley, B., Nilsson, J., Paolo, F. S., et al. (2020). Pervasive ice sheet mass loss reflects competing ocean and atmosphere processes. *Science*, *367*(6496), 1239-1242. https://doi.org/10.1126/science.aaz5845

Zheng, W., Pritchard, M. E., Willis, M. J., Tepes, P., Gourmelen, N., Benham, T. J., & Dowdeswell, J. A. (2018). Accelerating glacier mass loss on Franz Josef Land, Russian Arctic. *Remote Sensing of Environment,* 211, 357–375. https://doi.org/10.1016/j.rse.2018.04.004